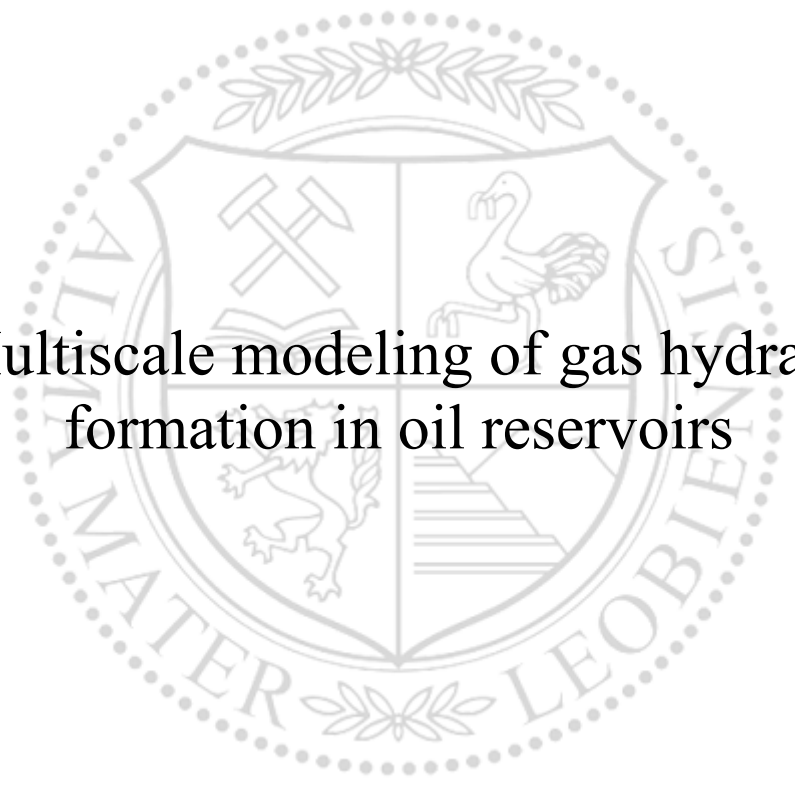




Chair of Reservoir Engineering

Master's Thesis



Multiscale modeling of gas hydrate
formation in oil reservoirs

Daniel Judmaier, BSc

May 2021

Daniel Judmaier

Master Thesis 2021

Supervisor: Dr. Luis Zerpa

Co-supervisor: Dr. Holger Ott

Multiscale modeling of gas hydrate formation in oil reservoirs

Declaration

I hereby declare that except where specific reference is made to the work of others, the contents of this dissertation are original and have not been published elsewhere. This dissertation is the outcome of my own work using only cited literature.

Erklärung

Hiermit erkläre ich, dass der Inhalt dieser Dissertation, sofern nicht ausdrücklich auf die Arbeit Dritter Bezug genommen wird, ursprünglich ist und nicht an anderer Stelle veröffentlicht wurde. Diese Dissertation ist das Ergebnis meiner eigenen Arbeit mit nur zitierter Literatur.

A handwritten signature in black ink that reads "Daniel Judmaier". The signature is written in a cursive style with a horizontal line underneath it.

Daniel Judmaier, 02 May 2021

Acknowledgements

I take great pleasure in thanking the following people without whom this unique master's program and this present thesis would not have been possible.

First of all, I would like to express my sincere gratitude and appreciation to Dr. Luis Zerpa for giving me the research opportunity at the Colorado School of Mines and for his consistent support and guidance throughout this project.

I would like to thank Dr. Holger Ott for establishing this master's program and his assistance in a very professional manner during this process.

I feel honored to have gotten input from many globally recognized professors and want to thank my thesis committee: Dr. Luis Zerpa, Dr. Holger Ott, and Dr. Xiaolong Yin.

I would like to acknowledge the researchers from the Center for Hydrate Research and the Center for Rock and Fluid Multiphysics at the Colorado School of Mines for their thoughtful comments and recommendations. A special thank you to Bianca Geranutti, whose work is the basis of this project, for her courtesy and for sharing her experiences.

I would like to thank the Petroleum Engineering Department staff from both my universities for their patience and support, particularly Bettina Matzer from the Montanuniversitaet Leoben and Denise Winn-Bower from the Colorado School of Mines.

Last but not least, I would like to deeply thank my family and friends for all their unconditional support in this very intense academic and private journey. I would especially like to recognize my father, Josef Rathschüller, for all his support and encouragement.

Abstract

Oftentimes, undersaturated oil reservoirs are subject to cold water injection to enhance the ultimate oil recovery of a field. During this process, the risk of gas hydrate formation that lowers the intrinsic permeability of a reservoir rock occurs if special thermodynamic conditions are met. Coreflooding experiments performed in previous work verified the possibility of gas hydrate formation in Bentheimer sandstone core samples saturated with live-oil during the injection of cold water. To further assess this process, the objective of this thesis was to numerically reproduce the laboratory experiments and extend the scope to different scales, namely to the pore scale, the laboratory coreflood scale, and the field scale.

Numerical models for two different core samples with different physical dimensions were created to simulate the conditions of gas hydrate formation during cold water injection experiments. The first model represented the large diameter core sample with the dimensions of 3 inches in diameter and 10 inches in length, and the second one represented the small diameter core sample with the dimensions of 1.5 inches in diameter and 12 inches in length. The models were fine-tuned to reproduce experimental results for different injection rates, temperatures, and salinities of the injected water.

The models that matched the waterfront location and solid saturation were upscaled to a four acres five-spot vertical-well pattern waterflooding operation. The model showed that the permeability reduction due to the formation of gas hydrates affects the waterflooding process performance. All the simulations have been performed with the commercial reservoir simulator STARS by Computer Modelling Group (CMG).

The results of this research showed that the waterfront location during the cold-water injection in the laboratory coreflooding experiments could be reproduced by tuning the models. Modifications of reservoir simulation models included changing capillary pressure relations and adjusting parameters of hydrate formation reactions. Pressure differential measurements that gave indirect information about the hydrate saturation formed in the experiments showed the same trend in the numerical models. Furthermore, the field scale simulations showed a significant permeability reduction due to the formation of hydrates.

Zusammenfassung

Untergesättigte Erdöllagerstätten werden oftmals einer Kaltwasserinjektion unterzogen, um die Gewinnung eines Feldes zu verbessern. Während dieses Prozesses besteht das Risiko einer Gashydratbildung, die die intrinsische Permeabilität einer Lagerstätte senkt, wenn spezielle thermodynamische Bedingungen erfüllt sind. Experimente aus einer früheren Arbeit bestätigten die Möglichkeit der Bildung von Gashydraten in ölgesättigten Bentheimer Sandsteinkernproben während der Injektion von kaltem Wasser. Um diesen Prozess weiter zu bewerten, bestand das Ziel dieser Arbeit darin, die Experimente numerisch zu reproduzieren und den Umfang auf verschiedene Skalen auszudehnen, nämlich auf die Porenskala, die Laborkernflutskala und die Feldskala.

Es wurden numerische Modelle für zwei verschiedene Kernproben mit unterschiedlichen physikalischen Abmessungen erstellt, um die Bedingungen der Gashydratbildung während der Kaltwasserinjektion zu simulieren. Das erste Modell stellte eine Kernprobe mit den Abmessungen von 3 Zoll im Durchmesser und 10 Zoll in der Länge und das zweite Modell stellte eine Kernprobe mit den Abmessungen von 1,5 Zoll im Durchmesser und 12 Zoll in der Länge dar. Die Modelle wurden fein abgestimmt, um experimentelle Ergebnisse für verschiedene Injektionsraten, Temperaturen und Salzgehalte des injizierten Wassers zu reproduzieren.

Die Modelle wurden dann auf die Feldskala, welche eine Fünf-Punkt-Kaltwasserinjektion simuliert, skaliert. Das Modell zeigte einen Effekt auf die Effizienz der Kaltwasserinjektion in der Verringerung der Permeabilität aufgrund der Bildung von Gashydraten. Alle Simulationen wurden mit dem kommerziellen Lagerstättensimulator STARS der Computer Modelling Group (CMG) durchgeführt.

Die Ergebnisse dieser Forschung zeigten, dass der Ort der Wasserfront während der Kaltwasserinjektion in den Labor-Kernflutversuchen durch Abstimmung der numerischen Modelle reproduziert werden konnte. Druckdifferenzmessungen, die indirekte Informationen über die in den Experimenten gebildete Gashydratsättigung liefern sollten, zeigten den gleichen Trend in den numerischen Modellen. Darüber hinaus zeigten die Simulationen im Feldmaßstab eine signifikante Verringerung der Permeabilität aufgrund der Bildung von Hydraten.

Table of Contents

Chapter 1.....	19
1.1 Background and Context.....	19
1.2 Scope and Objectives.....	22
1.3 Achievements.....	23
1.4 Thesis organization	24
Chapter 2.....	25
Chapter 3.....	31
3.1 Numerical Reservoir Simulator – CMG-STARs.....	32
3.2 Cartesian Core Setup.....	34
3.3 Radial Core Setup – Large Diameter Core Sample	34
3.4 Radial Core Setup – Small Diameter Core Sample	38
3.5 Field Scale Setup.....	41
Chapter 4.....	43
4.1 Experimental Coreflood Results	43
4.2 Analytical Waterflooding Solution Results	46
4.3 Numerical Coreflood Simulation Results	49
4.4 Discussion.....	67
Chapter 5.....	69
5.1 Summary	69
5.2 Evaluation	70
5.3 Future Work.....	70
Chapter 6.....	1

List of Figures

Figure 1.1 – Core photograph (Geranutti 2020).	20
Figure 2.1 – Hydrate structures: Structure I, Structure II, and Structure H (Tohidi Kalorazi and Anderson 2008).	26
Figure 2.2 – Hydrate stability zone.	27
Figure 2.3 – Seismic image showing a typical BSR (Meltser, Goldberg, and Guerin 1999).	28
Figure 2.4 – Pressure drawdown requirement.	29
Figure 3.1 – 3D representation of the Cartesian grid model.	34
Figure 3.2 – Water production, large diameter core.	36
Figure 3.3 – Oil production, large diameter core.	36
Figure 3.4 – 3D representation of the large diameter core sample in cylindrical coordinates.	37
Figure 3.5 – Water production, small diameter core.	39
Figure 3.6 – Oil production, small diameter core.	39
Figure 3.7 – 3D representation of the small diameter core sample in cylindrical coordinates.	40
Figure 3.8 – 3D representation of the field scale model.	41
Figure 4.1 – Waterfront location determination using compressional wave velocities (Geranutti 2020).	44
Figure 4.2 – Pressure differential in the temperature ramp of the experiments (Geranutti 2020).	45
Figure 4.3 – Injection ramp at (a) 2 °C and (b) 15 °C (Geranutti 2020).	45
Figure 4.4 – Relative permeability curves of oil and water.	47
Figure 4.5 – Fractional flow curve of water.	48
Figure 4.6 – Water saturation profile after 3.5 hours of injection.	49
Figure 4.7 – Waterfront location after 3.5 hours of injection in the Cartesian model.	50
Figure 4.8 - Waterfront location after 1 hour of injection in the large core radial model.	50
Figure 4.9 – Waterfront location after 3.5 hours of injection in the large core radial model.	51
Figure 4.10 – Capillary Pressure Curve.	52
Figure 4.11 – Waterfront location after 3.5 hours of injection in the large core radial model including the capillary pressure effect.	52
Figure 4.12 – Hydrate equilibrium curves for formation water, seawater, and freshwater.	53
Figure 4.13 – Surface for seawater.	54
Figure 4.14 – Surface for formation water.	55
Figure 4.15 – Hydrate concentration along the core for every temperature step, large diameter core.	56
Figure 4.16 – Hydrate saturation along the core for every temperature step, large diameter core.	57
Figure 4.17 – Predicted pressure differential for the temperature ramp, small diameter core.	57
Figure 4.18 – Pressure differential for the injection ramp at 2 °C with seawater injection, small diameter core.	58
Figure 4.19 – Pressure differential for the injection ramp at 15 °C with seawater injection, small diameter core.	58
Figure 4.20 – Hydrate saturation along the core for every temperature step, small diameter core.	59
Figure 4.21 – Permeability in k-direction along the core for every temperature step, small diameter core.	59
Figure 4.22 – Hydrate saturation along the core after the 3 °C temperature step with an increase by two orders of magnitude of the reaction frequency factor, small diameter core.	60
Figure 4.23 – Permeability in k-direction along the core after the 3 °C temperature step with an increase by two orders of magnitude of the reaction frequency factor, small diameter core.	61
Figure 4.24 – Hydrate saturation along the core after the 3 °C temperature step and keeping the core at constant 2 °C for 24 hours without injection or production, small diameter core.	61

Figure 4.25 – Hydrate saturation along the core for each temperature step simulating 24 hours, small diameter core.	62
Figure 4.26 – Pressure differential for the injection ramp at 2 °C for the 24 hours simulations, small diameter core.	63
Figure 4.27 – Water production in the field scale model.	63
Figure 4.28 – Bottomhole pressure of the injector wells.	64
Figure 4.29 – Solid concentration in the areal view after three years of injection.	65
Figure 4.30 – Solid concentration in the vertical view after three years of injection.	65
Figure 4.31 – Permeability distribution in the areal view after three years of injection.	66
Figure 4.32 – Permeability distribution in the vertical view after three years of injection.	66
Figure 5.1 – Micro CT slice of a sandstone sample in (a) dry and (b) SIH state (Shabaninejad, Middleton, and Fogden 2018).	71
Figure 5.2 – Lattice Boltzmann evaluation of intrinsic permeability with (a) 3D digital image, (b) schematic fluid flow, and (c) steady state velocity field (Fu et al. 2020).	72

List of Tables

Table 1.1 – Characteristic reservoir properties of the Wisting field	19
Table 1.2 – Physical properties of the core samples	20
Table 1.3 – Formation water and seawater composition	21
Table 1.4 – Experimental procedure for the large diameter coreflood	21
Table 1.5 – Experimental procedure for the small diameter coreflood.....	22
Table 3.1 – Composition of the oil	31
Table 3.2 – Grid size options, large diameter core	35
Table 3.3 – Reservoir parameters for the numerical models	35
Table 3.4 – Well constraints for the injection well, large diameter core	35
Table 3.5 – Well constraints for the production well, large diameter core	36
Table 3.6 – Water breakthrough times for the different grid options, large diameter core.....	37
Table 3.7 – Grid size options, small diameter core.....	38
Table 3.8 – Well constraints for the injection well, small diameter core.....	38
Table 3.9 – Well constraints for the production well, small diameter core	39
Table 3.10 – Water breakthrough times for the different grid options, small diameter core ...	40
Table 4.1 – Injection Ramp at 2 °C.....	46
Table 4.2 – Injection Ramp at 15 °C.....	46
Table 4.3 – Input parameters for the analytical Buckley-Leverett solution.....	46
Table 4.4 – Fitting parameters k1, k2, k3	55
Table 4.5 – Hydrate reaction parameters	55
Table 4.6 – Parameters for the conversion of hydrate concentration to hydrate saturation	56

Nomenclature

A	cross-sectional area	[m ²]
A	hydrate reaction frequency factor	[-]
Ad_i	adsorbed component i	[-]
c_{hyd}	hydrate concentration	[gmol/cm ³]
C_i	concentration factor	[-]
c_s	solid concentration	[gmol/cm ³]
D_{gi}	dispersibility of component i in gaseous phase	[m ² /s]
D_{oi}	dispersibility of component i in oleic phase	[m ² /s]
D_{wi}	dispersibility of component i in aqueous phase	[m ² /s]
$\frac{dc_{hyd}}{dt}$	hydrate formation rate	[gmol/cm ³ .min]
$\frac{df_w}{dS_w}$	derivative of fractional flow of water	[-]
$\frac{\partial}{\partial t}$	time derivative	[-]
E_{ak}	activation energy	[J/gmol]
f_w	fractional flow of water	[-]
H_g	enthalpy of gas	[J/kg]
H_o	enthalpy of oil	[J/kg]
H_w	enthalpy of water	[J/kg]
K	hydrate equilibrium deviation rate	[-]
K	thermal conductivity	[W/(m.K)]

K_i^{go}	phase equilibrium ratio of gas and oil for component i	[-]
K_i^{ow}	phase equilibrium ratio of oil and water for component i	[-]
K_i^{gw}	phase equilibrium ratio of gas and water for component i	[-]
$k1$	K value coefficient	[-]
$k2$	K value coefficient	[-]
$k3$	K value coefficient	[-]
k_{ro}	relative permeability of oil	[-]
k_{rw}	relative permeability of water	[-]
$k_{ro,max}$	end-point relative permeability of oil	[-]
$k_{rw,max}$	end-point relative permeability of water	[-]
M_{hyd}	molecular weight of hydrates	[g/gmol]
n_o	Brooks-Corey coefficient for oil	[-]
n_w	Brooks-Corey coefficient for water	[-]
P	pressure	[Pa]
q_{inj}	injection rate	[cm ³ /min]
q_t	total rate	[m ³ /s]
q_{gk}	gas well phase rate	[m ³ /s]
q_{ok}	oil well phase rate	[m ³ /s]
q_{wk}	water well phase rate	[m ³ /s]
R	universal constant	[J/gmol.K]

S_{hyd}	hydrate saturation	[-]
S_g	gas saturation	[-]
S_o	oil saturation	[-]
S_w	water saturation	[-]
S_{or}	residual oil saturation	[-]
S_{wc}	connate water saturation	[-]
T	temperature	[°C]
t	time	[s]
U_g	internal energy of gas	[J]
U_o	internal energy of oil	[J]
U_s	internal energy of solid	[J]
U_r	energy per rock volume	[J]
U_w	internal energy of water	[J]
V	volume	[m ³]
w_i	concentration of component i in aqueous phase	[-]
x	distance	[m]
x_i	concentration of component i in oleic phase	[-]
y_i	concentration of component i in gaseous phase	[-]
ΔE	activation energy	[J/gmol]
ΔT	temperature gradient	[K]

Δw_i	change in concentration of component i in aqueous phase	[-]
Δx_i	change in concentration of component i in oleic phase	[-]
Δy_i	change in concentration of component i in gaseous phase	[-]
μ_o	oil viscosity	[cp]
μ_w	water viscosity	[cp]
ρ_{hyd}	hydrate density	[g/cm ³]
ρ_w	water density	[g/cm ³]
ϕ	porosity	[-]
ϕ_f	fluid porosity	[-]
ϕ_v	void porosity	[-]

Abbreviations

BSR	bottom simulating reflector
CMG	Computer Modelling Group
CT	computer tomography
HSZ	hydrate stability zone
LBM	Lattice Boltzmann Method
NMR	nuclear magnetic resonance
PVT	pressure, volume, and temperature
SIH	spontaneous imbibition of high salinity brine

Chapter 1

Introduction

This master's thesis is about the numerical modeling of gas hydrate formation in oil reservoirs on different scales. It is written at the Colorado School of Mines as part of the double degree master's program with the focus on Reservoir Management in cooperation with the Montanuniversitaet Leoben.

1.1 Background and Context

The formation of gas hydrates in oil saturated core samples has been investigated experimentally by Bianca Geranutti in her master's thesis in 2020 using reservoir parameters from the Wisting field located in the Barents Sea offshore Norway. Multiphysics measurements including electrical conductivity, strain, temperature, and elastic wave velocity, detected the formation of gas hydrates after specific times of water injection in the coreflood experiments.

The characteristic reservoir properties of the field are summarized in Table 1.1 and represent the operating conditions and parameters for the experiments.

Table 1.1 – Characteristic reservoir properties of the Wisting field

Parameter	Value
Temperature [°C]	17.8
Pressure [bar]	71.9
Bubble point [bar]	68.6
Oil gravity [°API]	38.3
Oil viscosity [cp]	2.452
Oil formation volume factor [m ³ /sm ³]	1.097
Gas-oil ratio [sm ³ /sm ³]	44.2

Wettability	Neutral
Porosity [%]	21.5-26.1
Permeability [md]	1760-3960
Irreducible water saturation [%]	5-10
Irreducible oil saturation [%]	5.1-20.8

Due to the unavailability of formation core samples, Bentheimer sandstone core samples, which resemble the properties of the formation, have been used in the experiments. The physical properties of the core samples are summarized in Table 1.2.

Table 1.2 – Physical properties of the core samples

Parameter	Value
Density [g/cm ³]	2
Porosity [%]	25.5
Permeability [md]	2750
Median grain size [nm]	235-350

In total, 12 strain gauges, nine electrode rings, 20 P-wave crystals, 20 S-wave crystals, and 12 temperature sensors were installed on the core samples for the multiphysics measurements. The final instrumentation of the cores is shown in Figure 1.1.



Figure 1.1 – Core photograph (Geranutti 2020).

The experiments were performed on three core samples that differ in physical dimensions. The first one was the tiny coreflood, with the core dimensions of 1.5 inches in diameter and 2 inches in length, the second one was the large diameter coreflood, with the core dimensions of 3 inches in diameter and 10 inches in length, and the third one was the small diameter coreflood, with the core dimensions of 1.5 inches in diameter and 12 inches in length.

The experimental procedure followed a core saturation with formation fluids before cold seawater was injected in several different temperature steps for certain times. The formation water and seawater composition are summarized in Table 1.3 and the cooling and injection steps for the large diameter and small diameter core samples are shown in Table 1.4 and Table 1.5. Due to the small physical dimensions and lack of fluid flow, the tiny coreflood experiments are not subject to the numerical modeling in this thesis, that is why they are not further described here.

Table 1.3 – Formation water and seawater composition

Salt type	Formation water composition [g/l]	Seawater composition [g/l]
NaCl	56.930	25.690
MgCl ₂ * 6H ₂ O	8.450	11.040
CaCl ₂ * 2H ₂ O	7.250	1.560
SrCl ₂ * 6H ₂ O	0.736	0.024
BaCl ₂ * 2H ₂ O	0.697	-
KCl	0.243	0.784
NaBO ₂ * 4H ₂ O	0.043	0.201
Na ₂ SO ₄	0.030	-

Table 1.4 – Experimental procedure for the large diameter coreflood

1	Cool down to 15 °C		No injection
2	Inject for 30 minutes	T = 15 °C	q _{inj} = 0.2 cm ³ /min
3	Acoustic/electric measurements	T = 15 °C	No injection
4	Cool down to 12 °C		No injection
5	Inject for 60 minutes	T = 12 °C	q _{inj} = 0.2 cm ³ /min
6	Acoustic/electric measurements	T = 12 °C	No injection
7	Cool down to 10 °C		No injection
8	Inject for 60 minutes	T = 10 °C	q _{inj} = 0.2 cm ³ /min
9	Acoustic/electric measurements	T = 10 °C	No injection
10	Cool down to 8 °C		No injection
11	Inject for 20 minutes	T = 8 °C	q _{inj} = 0.2 cm ³ /min
12	Acoustic/electric measurements	T = 8 °C	No injection
13	Cool down to 7 °C		No injection
14	Inject for 20 minutes	T = 7 °C	q _{inj} = 0.2 cm ³ /min
15	Acoustic/electric measurements	T = 7 °C	No injection
16	Cool down to 6 °C		No injection
17	Inject for 20 minutes	T = 6 °C	q _{inj} = 0.2 cm ³ /min
18	Acoustic/electric measurements	T = 6 °C	No injection

22	Cool down to 4 °C		No injection
23	Inject for 20 minutes	T = 4 °C	$q_{inj} = 0.2 \text{ cm}^3/\text{min}$
24	Acoustic/electric measurements	T = 4 °C	No injection
25	Cool down to 3 °C		No injection
26	Inject for 20 minutes	T = 3 °C	$q_{inj} = 0.2 \text{ cm}^3/\text{min}$
27	Acoustic/electric measurements	T = 3 °C	No injection
28	Cool down to 2 °C		No injection
29	Inject for 20 minutes	T = 2 °C	$q_{inj} = 0.2 \text{ cm}^3/\text{min}$
30	Acoustic/electric measurements	T = 2 °C	No injection

Table 1.5 – Experimental procedure for the small diameter coreflood

1	Cool down to 15 °C		No injection
2	Inject for 30 minutes while measuring	T = 15 °C	$q_{inj} = 0.05 \text{ cm}^3/\text{min}$
3	Cool down to 11 °C		No injection
4	Inject for 30 minutes while measuring	T = 11 °C	$q_{inj} = 0.05 \text{ cm}^3/\text{min}$
5	Cool down to 8 °C		No injection
6	Inject for 30 minutes while measuring	T = 8 °C	$q_{inj} = 0.05 \text{ cm}^3/\text{min}$
7	Cool down to 7 °C		No injection
8	Inject for 30 minutes while measuring	T = 7 °C	$q_{inj} = 0.05 \text{ cm}^3/\text{min}$
9	Cool down to 6 °C		No injection
10	Inject for 30 minutes while measuring	T = 6 °C	$q_{inj} = 0.05 \text{ cm}^3/\text{min}$
11	Cool down to 5 °C		No injection
12	Inject for 30 minutes while measuring	T = 5 °C	$q_{inj} = 0.05 \text{ cm}^3/\text{min}$
13	Cool down to 4 °C		No injection
14	Inject for 30 minutes while measuring	T = 4 °C	$q_{inj} = 0.05 \text{ cm}^3/\text{min}$
15	Cool down to 3 °C		No injection
16	Inject for 30 minutes while measuring	T = 3 °C	$q_{inj} = 0.05 \text{ cm}^3/\text{min}$
17	Cool down to 2 °C		No injection
18	Inject for 30 minutes while measuring	T = 2 °C	$q_{inj} = 0.05 \text{ cm}^3/\text{min}$

1.2 Scope and Objectives

Comprehensive knowledge and research on natural occurrences of gas hydrates in shallow sediments exist but only little is known when it comes to gas hydrate formation in oil reservoirs. The additional oil phase makes the problem that already deals with multiphase fluid flow in porous media more complicated. The objectives of this master's thesis are the evaluation of gas hydrate formation using numerical simulation in terms of the hydrate formation reaction and resulting permeability effects. This evaluation will be performed on different scales, namely on

the pore scale, the laboratory core flooding scale, and the field scale. A successful evaluation will lead to the ability to answer the research questions of how gas hydrates form in undersaturated oil reservoirs, how they are distributed in the porous network of the reservoir rock, and which effects with respect to the permeability changes result. This will ultimately lead to an increasing awareness of waterflooding projects in reservoirs where hydrates can occur. To accomplish these objectives, the research is divided into four main tasks:

- Task 1 is to create a reservoir simulation model that is able to reproduce results from an experimental study of gas hydrate formation in oil-saturated core samples during water injection (Geranutti 2020). The experiments were performed on Bentheimer sandstone core samples using reservoir fluids from the Wisting field located offshore Norway.
- Task 2 is the investigation of how the formation of hydrates will affect the permeability.
- Task 3 is the upscaling of the model to a field level to get information of the behavior of hydrate formation in an oil reservoir.
- Task 4 is the distribution of gas hydrates at the pore scale that was inferred from experimental measurements using pore scale modeling, to probe a realistic distribution of hydrates in the pore space.

1.3 Achievements

Numerical reservoir simulation models in cylindrical coordinates have been created that are able to reproduce the waterfront distribution observed in previously done coreflood experiments of Bentheimer sandstone core samples.

The models furthermore are able to show gas hydrate formation throughout the core samples at certain times and temperatures during cold water injection that was observed in the experiments and give information about the computed saturation distributions.

Moreover, the relationship of hydrates and resulting permeability reduction of the core samples has been determined using the numerical models.

The information from the fine-tuning of the numerical models to match the experimental coreflood results has been used to create a five-spot pattern numerical field scale waterflooding operation which gives information about the permeability reduction in the field when hydrates are formed.

1.4 Thesis organization

This thesis consists of six main chapters. The summary of each individual chapter is presented as follows:

- Chapter 1 presents the background and related previous work, explains the objectives of the research, summarizes the main achievements, and shows the organization of the thesis.
- Chapter 2 introduces the theoretical background in form of a literature review related to the research.
- Chapter 3 explains the methodology of the numerical setup of the cores and the field.
- Chapter 4 presents relevant results from the coreflood experiments and the results from the analytical as well as from the numerical solutions with a discussion of the work.
- Chapter 5 concludes the research and gives an outline of the proposed future work.
- Chapter 6 states the references used.

Chapter 2

Literature Review

Gas clathrates, or often called gas hydrates, are metastable, solid, crystalline clathrate inclusion compounds that form under special conditions of low temperatures and high pressures when water molecules encounter gaseous guest molecules. The natural stability of gas hydrates is determined by the thermodynamic conditions of the system and the composition and properties of the water and the gas. Hydrogen-bonded water forms crystalline lattice cages in which gas molecules at a size of 0.35 nm to 0.9 nm are trapped (Makogon et al. 2004).

Although gas hydrates seem to be ice-like structures, they can exist under elevated pressure conditions above the freezing point of 0 °C. The structure that gas hydrates form depends on the size of the entrapped guest molecule but can mainly be distinguished into a body-centered cubic structure (Structure I) that is able to trap guest molecules smaller than propane, and a diamond lattice within a cubic framework (Structure II) that is able to trap molecules bigger than ethane but smaller than pentane (Sloan 1991). Figure 2.1 shows these two main structures and a third one, Structure H, that requires the presence of a smaller helper molecule in combination with a large, heavy molecule (Tohidi Kalorazi and Anderson 2008).

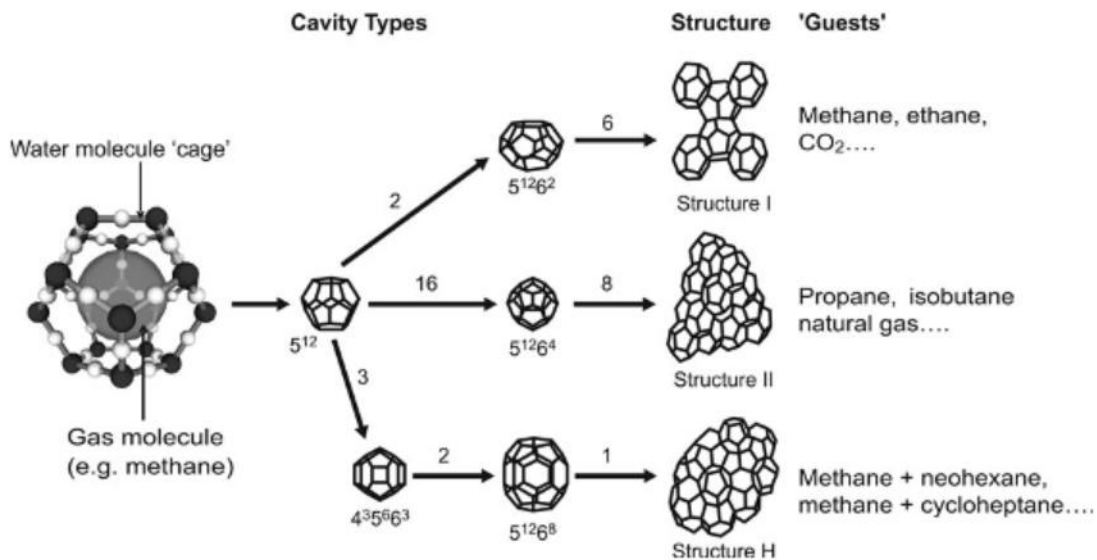


Figure 2.1 – Hydrate structures: Structure I, Structure II, and Structure H (Tohidi Kalorazi and Anderson 2008).

The conditions under which gas hydrates exist naturally are usually identified in sediments of the outer continental margin of oceans and polar areas that show a continuous permafrost. The main regions are the Pacific Ocean, Indian Ocean, Atlantic Ocean, Arctic Ocean, Antarctica, some inland seas and lakes, and continental regions (Kvenvolden and Lorenson 2001).

Generally, stable hydrate conditions can be found in areas that show a sufficiently cold environment in permafrost zones and offshore where water depth is usually greater than 300 m (Reichel and Gallagher 2014). However, only about 2% of gas hydrates are found in permafrost zones on land and 98% of gas hydrates are located offshore.

Hydrate bearing sediments may reach a thickness of hundreds of meters to even more than one kilometer in some areas (Makogon et al. 2004). Thereby, the saturation of gas hydrates in those layers can be highly variable. The range is from 0%, where only pure water is the mobile phase, to as high as 70% in some zones of interest (Hancock, Boswell, and Collett 2019). Furthermore, because the low capillary pressure in the pores of coarse-grained sandstone allows the migration of gas and the formation of hydrates, reservoirs that show these physical properties are preferred by gas hydrates (Collett 2013).

Identifying gas hydrates leads to seismic reflection profiling where anomalous reflections result from the acoustic difference between the sediments within the hydrate stability zone (HSZ) that contains gas hydrates and the sediments below the HSZ that contains gases but do not show hydrates (Kvenvolden and Lorenson 2001). Figure 2.2 shows the hydrate stability zone

dependent on the temperature below the mudline of the seafloor, which is the zone between the hydrate stability temperature and the geothermal gradient of the area.

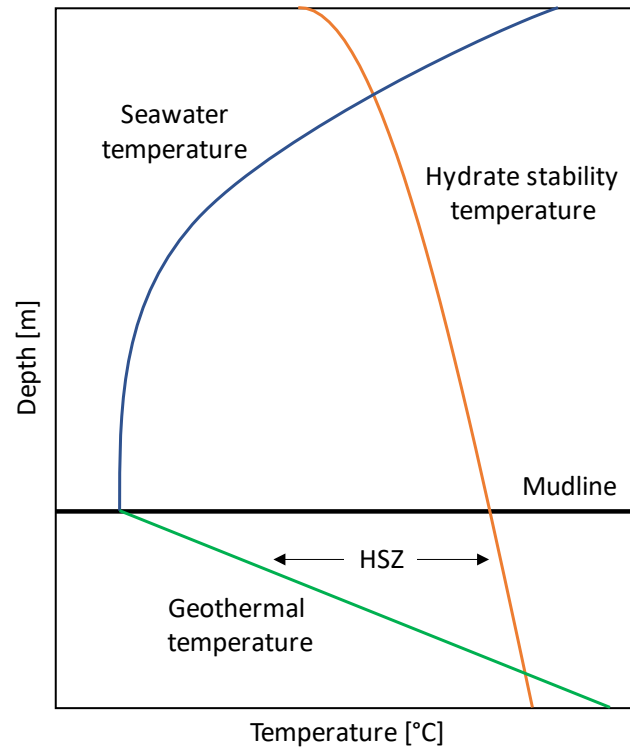


Figure 2.2 – Hydrate stability zone.

Bottom Simulating Reflectors (BSRs) are used in the seismic process of identifying the bottom of the gas hydrate stability zone (Reichel and Gallagher 2014). They are reflections of the seismic signal parallel to the seafloor caused by the sharp contrast of elastic waves between the hydrate bearing sediment and the underlying gas or brine bearing sediment (Ecker, Dvorkin, and Nur 1996). A seismic image showing the identification of gas hydrates through BSRs can be seen in Figure 2.3.

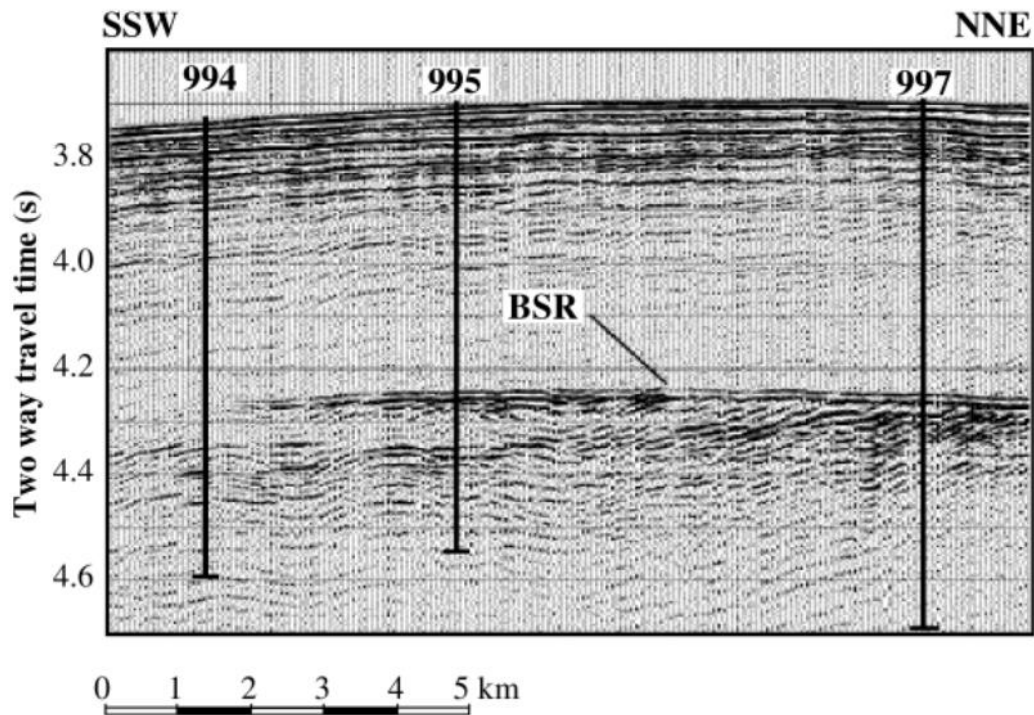


Figure 2.3 – Seismic image showing a typical BSR (Meltser, Goldberg, and Guerin 1999).

At the pore scale, nuclear magnetic resonance (NMR) measurements in the laboratory and wireline formation testing in the field help to identify and characterize gas hydrate bearing reservoirs. A gas hydrate estimation in the formation can be derived from downhole electric resistivity and acoustic velocity log data (Collett 2013).

The potential of gas hydrates in terms of energy resource is enormous. One m^3 of water is able to entrap 164 m^3 of methane at standard conditions in the hydrate state. This huge storage capacity of gas hydrates can be explained by the fact that gas hydrate deposits can also form from dissolved gas in the bulk water phase rather than just from free gas in the porous media. However, the amount of the dissolved gas in the reservoir water depends on the temperature and pressure conditions, water and gas migration routes into the layers, rate of gas diffusion, tectonic transitions, and the composition of the gas and water phases (Makogon et al. 2004). Also, gas hydrates that entrap methane as guest molecules show a ten times higher energy density than that of other unconventional gas sources such as coal bed methane and tight sands, and a two to five times higher energy density than that of conventional natural gas.

On the contrary, methane in gas hydrates shows the potential of being a greenhouse gas that enhances climate change when being present in the earth's atmosphere. The potential of global warming is 20 times higher than that of CO_2 , but the half-life in the atmosphere is very short. Therefore, the overall effects on global warming are much less than that of CO_2 emissions.

Another hazard of gas hydrate accumulations is the destabilization of the seafloor which affects structures such as petroleum production platforms and pipelines that are tied to the seafloor (Kvenvolden and Lorenson 2001).

If wellbore or pipeline temperatures drop at a certain flowing pressure due to the reservoir configuration or possible Joule-Thompson effects while producing at high rates, gas hydrates may form which leads to problems concerning flow assurance. This includes gas production with extremely high water cuts, low operating pressures and temperatures, a reformation of gas hydrates, and erosion with solids production at high gas velocities. Furthermore, a gas well that deals with the formation of gas hydrates requires artificial lift systems to remove the hydrostatic head of the water to initiate dissociation and to remove the water accumulation in the wellbore at a well restart. Getting rid of the solid gas hydrates that may clog wellbores and pipelines can be accomplished by hydrate dissociation (Hancock, Boswell, and Collett 2019). This requires a high-pressure drawdown to reach the boundary of the hydrate stability curve which can be seen in Figure 2.4.

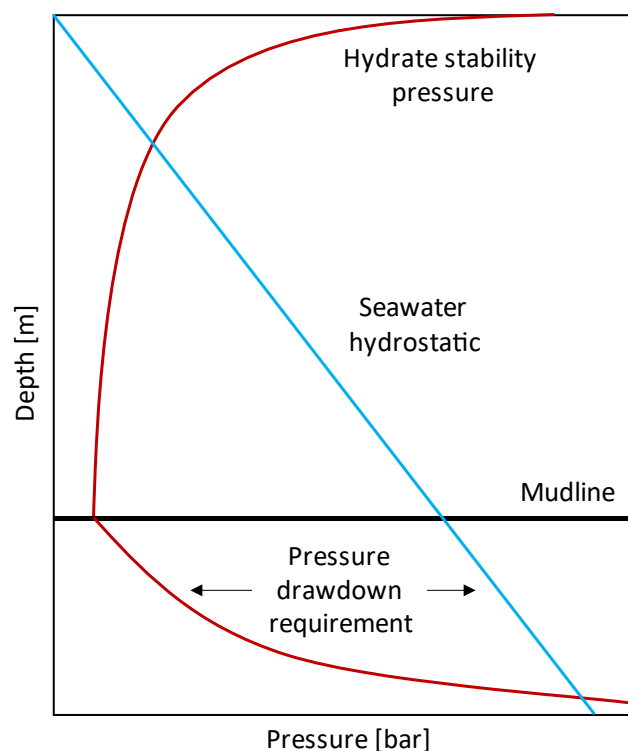


Figure 2.4 – Pressure drawdown requirement.

Because of the difficulties in measuring the hydrate stability zone if oil is present and the compositional representation of these systems, only little information with respect to the

formation and stability of gas hydrates in oil reservoirs is known. Therefore, the study of the thermodynamic, as well as kinetic behavior of hydrates in oil bearing formations, is of great interest. In these systems, the components that are responsible for forming hydrates are distributed in the vapor, oil, and aqueous phases. Studies have also shown that high water cuts can shift the hydrate stability zone to lower temperatures at pressures above the bubble point (Mohammadi et al. 2006).

Once hydrates are present in the porous reservoir rock, a permeability reduction effect can be observed as the hydrates clog the pore channels (Delli and Grozic 2013).

Chapter 3

Numerical Setup

In the numerical study, reservoir models representing the Bentheimer sandstone core samples are set up. The software that is used is the reactive flow simulator STARS (by Computer Modeling Group, CMG). The models are initially oil saturated with the composition obtained from PVT measurements in the experimental study summarized in Table 3.1.

Table 3.1 – Composition of the oil

Component	Value [%mol]
CO ₂	2.23
C1	24.48
C2	2.44
C3	2.34
iC4	1.17
nC4	1.77
Neo-C5	1.39
C6	3.28
C7	5.53
C8	8.07
C9	5.17
C10-C12	10.58
C13-C14	5.83
C15-C16	4.78
C17-C19	5.54
C20-C22	3.34
C23-C27	3.53
C28-C34	2.95

C35-C44	2.17
C45-C80	1.56

3.1 Numerical Reservoir Simulator – CMG-STARS

The numerical reservoir simulator CMG-STARS uses two conservation equations to account for fluid and thermal changes in the reservoir: conservation of mass and conservation of energy.

The mass conservation equation for each component i considers multiple phases as:

$$\begin{aligned}
V \frac{\partial}{\partial t} [\phi_f (\rho_w S_w w_i + \rho_o S_o x_i + \rho_g S_g y_i) + \phi_v A d_i] \\
= \rho_w S_w w_i + \rho_o S_o x_i + \rho_g S_g y_i + \phi \rho_w D_{wi} \Delta w_i + \phi \rho_o D_{oi} \Delta x_i \\
+ \phi \rho_g D_{gi} \Delta y_i + \rho_w q_{wk} w_i + \rho_o q_{ok} x_i + \rho_g q_{gk} y_i
\end{aligned} \quad (3.1)$$

where V is the total volume of the grid block, ϕ_f is the fluid porosity, ϕ_v is the void porosity, ρ_w is the density of water, ρ_o is the density of oil, ρ_g is the density of gas, S_w is the water saturation, S_o is the oil saturation, S_g is the gas saturation, w_i is the concentration of component i in the aqueous phase, x_i is the concentration of component i in the oleic phase, y_i is the concentration of component i in the gaseous phase, Δw_i is the change in concentration of component i in aqueous phase, Δx_i is the change in concentration of component i in oleic phase, Δy_i is the change in concentration of component i in gaseous phase, $A d_i$ is the adsorbed component i , q_{wk} is the water well phase rate, q_{ok} is the oil well phase rate, q_{gk} is the gas well phase rate, D_{wi} is the dispersibility of component i in aqueous phase, D_{oi} is the dispersibility of component i in oleic phase, D_{gi} is the dispersibility of component i in gaseous phase, and ϕ is the absolute porosity.

The energy conservation equation considering multiple phases is:

$$\begin{aligned}
V \frac{\partial}{\partial t} [\phi_f (\rho_w S_w U_w + \rho_o S_o U_o + \rho_g S_g U_g) + \phi_v c_s U_s + (1 - \phi) U_r] \\
= \rho_w V_w H_w + \rho_o V_o H_o + \rho_g V_g H_g + K \Delta T + \rho_w q_{wk} H_w \\
+ \rho_o q_{ok} H_o + \rho_g q_{gk} H_g
\end{aligned} \quad (3.2)$$

where V is the total volume of the grid block, ϕ_f is the fluid porosity, ϕ_v is the void porosity, ρ_w is the density of water, ρ_o is the density of oil, ρ_g is the density of gas, S_w is the water saturation, S_o is the oil saturation, S_g is the gas saturation, U_w is the internal energy of water,

U_o is the internal energy of oil, U_g is the internal energy of gas, U_s is the internal energy of the solid phase, U_r is the energy per rock volume, c_s is the solid concentration, H_w is the water enthalpy, H_o is the oil enthalpy, H_g is the gas enthalpy, K is the thermal conductivity, ΔT is the temperature gradient, q_{wk} is the water well phase rate, q_{ok} is the oil well phase rate, q_{gk} is the gas well phase rate, and ϕ is the absolute porosity.

The phase equilibrium in CMG-STAR3 is specified via phase equilibrium ratios (K-values) that are directly input as functions of pressure, temperature, and composition. The definition of those K-values is:

$$K_i^{gw} = \frac{y_i}{w_i}, K_i^{go} = \frac{y_i}{x_i}, K_i^{ow} = \frac{x_i}{w_i} \quad (3.3)$$

where K_i^{gw} is the phase equilibrium ratio of gas and water for component i , K_i^{go} is the phase equilibrium ratio of gas and oil for component i , K_i^{ow} is the phase equilibrium ratio of oil and water for component i , w_i is the concentration of component i in the aqueous phase, x_i is the concentration of component i in the oleic phase, and y_i is the concentration of component i in the gaseous phase.

CMG-STAR3 thereby groups components as water-like, oil-like, and non-condensable gases for efficiency purposes.

Furthermore, chemical reactions are modeled in CMG-STAR3 as source/sink terms, conserving the moles of each reaction component and energy. However, the reaction stoichiometry must be mass conserving in order for the reaction to make physically sense. The general expression for the reaction kinetics, which determines the speed of a reaction is:

$$r_k = r_{rk} * \exp\left(-\frac{E_{ak}}{RT}\right) * \prod_{i=1}^{n_c} C_i^{e_k} \quad (3.4)$$

where E_{ak} is the activation energy that determines the temperature dependence of the reaction r_k and C_i is the concentration factor for the reacting component i , defined as:

$$C_i = \phi_f \rho_j S_j x_{ij} \quad j = w, o, g \quad (3.5)$$

where j is the phase in which component i is reacting and x_{ij} is the mole fraction of water, oil, or gas (Computer Modelling Group Ltd. 2016).

3.2 Cartesian Core Setup

A numerical model in Cartesian coordinates has been created in previous work by Bianca Geranutti in her master's thesis in 2020. It represents the large core sample with a diameter of 3 inches and a length of 10 inches. The model consists of 150 blocks in z-direction that sum up to 10 inches in length and are equally distributed over one cell on the whole area of the core. It includes a producer and an injector well in the center of the grid. The producer is perforated in the bottom cell of the grid and the injector is perforated in the top cell of the grid. This simulates water injection from the bottom and the resulting oil production in the top. The 3D representation of the model can be seen in Figure 3.1.

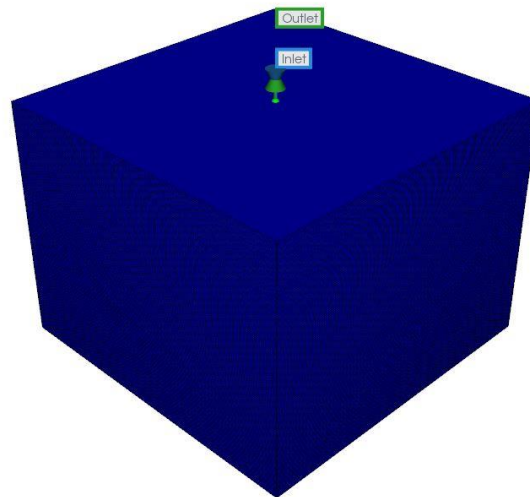


Figure 3.1 – 3D representation of the Cartesian grid model.

3.3 Radial Core Setup – Large Diameter Core Sample

The first numerical model that has been created in the framework of the present thesis is a radial grid model with a diameter of 3 inches and a length of 10 inches representing the large core sample from the experiments.

3.3.1 Sensitivity Analysis

A sensitivity analysis gives information about the optimum distribution of cells in the different dimensions of the 3D model. Three different grid size possibilities have been set up. The settings for that are summarized in Table 3.2.

Table 3.2 – Grid size options, large diameter core

Parameter	Case-1	Case-2	Case-3
Number of blocks in i-direction	10	10	10
Size of the blocks in i-direction [cm]	0.381	0.381	0.381
Number of blocks in j-direction	10	10	10
Size of the blocks in j-direction [°]	36	36	36
Number of blocks in k-direction	10	50	100
Size of the blocks in k-direction [cm]	2.54	0.508	0.254

These settings lead to three different models which differ in the number of blocks in k-direction.

Table 3.3 represents the reservoir parameters of the Wisting field and are the same for all the models.

Table 3.3 – Reservoir parameters for the numerical models

Parameter	Value
Reservoir temperature [°C]	17.8
Reservoir pressure [bar]	79.29
Porosity [-]	0.26
Permeability [md]	2750
Initial water saturation [-]	0.1
Initial oil saturation [-]	0.9

Furthermore, two wells, one producer and one injector, are created in the model to simulate pure water injection from the bottom of the core which results in oil production at the top of the core. The wells are perforated in the center of the core and the well constraints for the injector are listed in Table 3.4 and for the producer in Table 3.5.

Table 3.4 – Well constraints for the injection well, large diameter core

Parameter	Value
Perforation [i, j, k]	1, 1, k_{\max}
Well radius [cm]	0.15
Injection fluid	Water
Injection volume [cm ³ /min]	0.2
Injection temperature [°C]	8

Table 3.5 – Well constraints for the production well, large diameter core

Parameter	Value
Perforation [i, j, k]	1, 1, 1
Well radius [cm]	0.15
Minimum bottomhole pressure [kPa]	7190
Stop constraint if water production reaches 0.2 cm ³ /min	

Figure 3.2 and Figure 3.3 show the result of the water and oil versus time, respectively. These two figures are used to determine the optimum grid for further simulations.

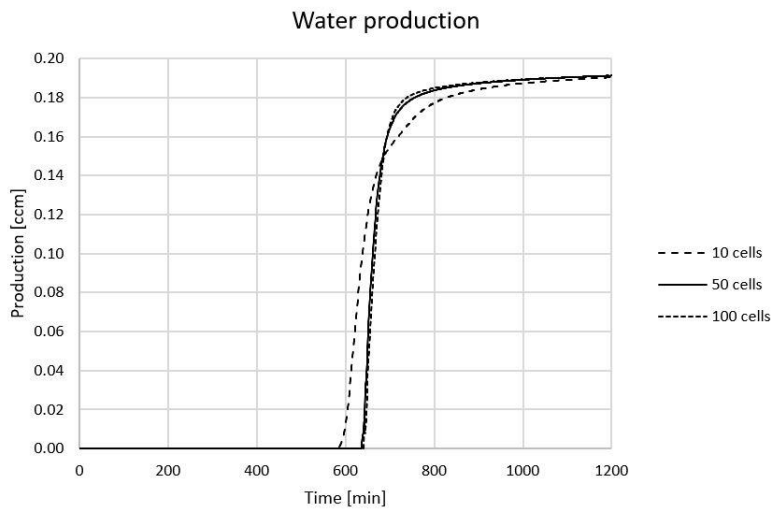


Figure 3.2 – Water production, large diameter core.

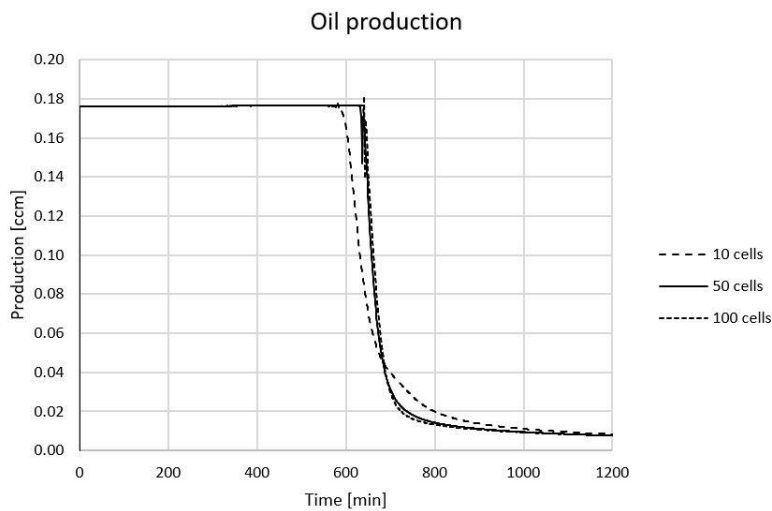


Figure 3.3 – Oil production, large diameter core.

It can be seen from the figures that the grid with 10 cells in k-direction shows a high numerical dispersion, whereas the grids with 50 cells and 100 cells, respectively, nearly show the same results. In fact, the difference in water breakthrough time in the grid with 50 cells and 100 cells is less than 1% but the simulation time is a lot longer for the 100 cells option. Therefore, the model option with 50 grid cells in k-direction is chosen for further simulations. The water breakthrough times are summarized in Table 3.6.

Table 3.6 – Water breakthrough times for the different grid options, large diameter core

Number of blocks [k]	Block size k [cm]	Water BT [hrs]
10	2.54	9.67
50	0.508	10.60
100	0.254	10.68

A 3D representation of the large core sample using the above-described parameters can be seen in Figure 3.4.

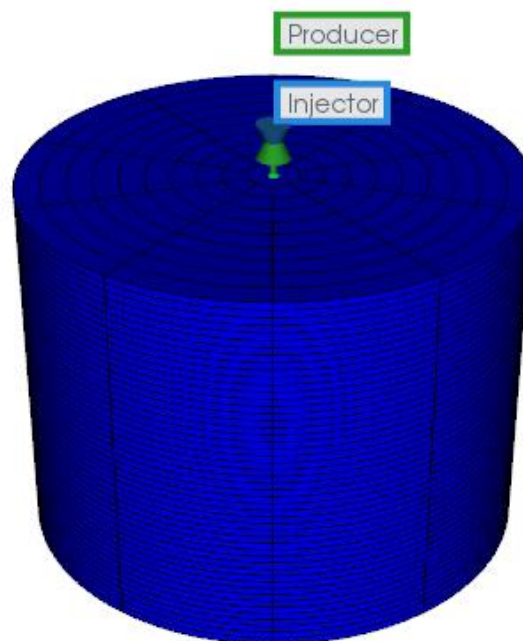


Figure 3.4 – 3D representation of the large diameter core sample in cylindrical coordinates.

3.4 Radial Core Setup – Small Diameter Core Sample

The second numerical model that has been created represents the small diameter core sample from the experiments with the physical dimensions of 1.5 inches in diameter and 12 inches in length.

3.4.1 Sensitivity Analysis

Four different grid size possibilities have been set up to determine the optimum distribution of cells in the model using a sensitivity analysis. The settings for that are summarized in Table 3.7.

Table 3.7 – Grid size options, small diameter core

Parameter	Case-1	Case-2	Case-3	Case-4
Number of blocks in i-direction	10	10	10	10
Size of the blocks in i-direction [cm]	0.1905	0.1905	0.1905	0.1905
Number of blocks in j-direction	10	10	10	10
Size of the blocks in j-direction [°]	36	36	36	36
Number of blocks in k-direction	10	50	100	150
Size of the blocks in k-direction [cm]	3.048	0.6096	0.3048	0.2032

These parameters lead to four different models which differ in the number of blocks in k-direction. The reservoir parameters are the same as for the large diameter core sample summarized in Table 3.3

Also, in this model, two wells, one producer and one injector, are created and perforated in the center of the model for water injection from the bottom of the core and oil production at the top of the core. The well constraints differ in the injection volume for the injector and the stop constraint for the producer with respect to the large diameter core model and are listed in Table 3.8 and in Table 3.9.

Table 3.8 – Well constraints for the injection well, small diameter core

Parameter	Value
Perforation [i, j, k]	1, 1, k_{\max}
Well radius [cm]	$7.9 * 10^{-4}$
Injection fluid	Water
Injection volume [cm ³ /min]	0.05
Injection temperature [°C]	8

Table 3.9 – Well constraints for the production well, small diameter core

Parameter	Value
Perforation [i, j, k]	1, 1, 1
Well radius [cm]	$7.9 * 10^{-4}$
Minimum bottomhole pressure [kPa]	7190
Stop constraint if water production reaches $0.05 \text{ cm}^3/\text{min}$	

Figure 3.5 shows the water production at the location of the production well versus time and Figure 3.6 shows the oil production versus time. These two figures are used to determine the optimum grid for further simulations.

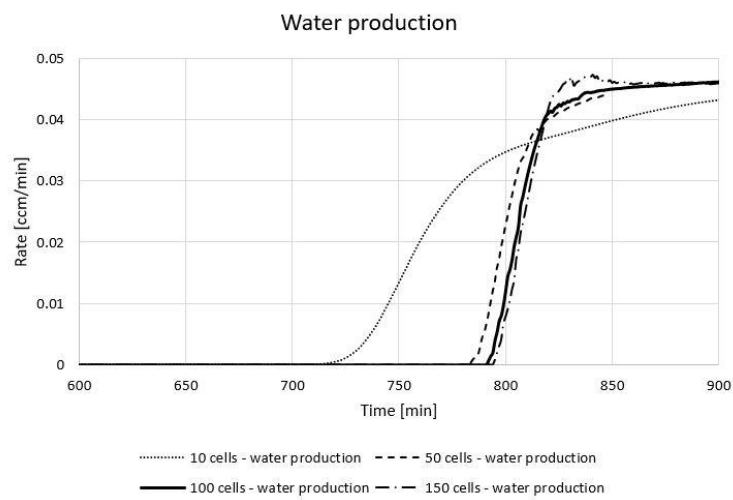


Figure 3.5 – Water production, small diameter core.

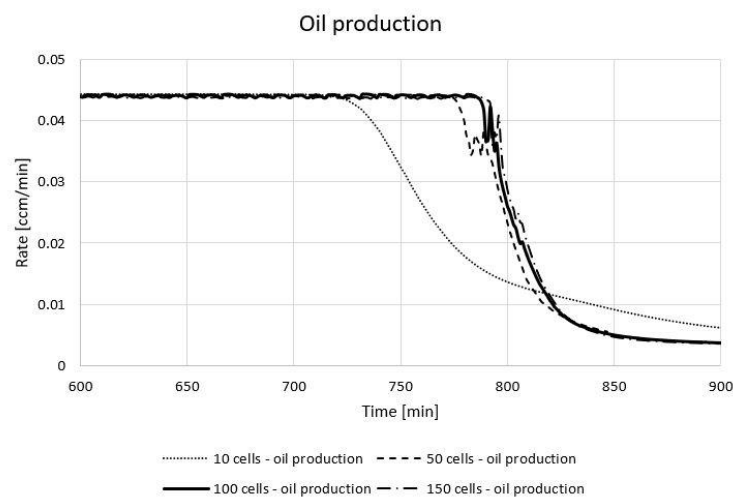


Figure 3.6 – Oil production, small diameter core.

The grid with 10 cells in k-direction and the grid option with 50 cells in k-direction both show a high numerical dispersion, whereas the grids with 100 cells and 150 cells, respectively, nearly show the same results. The difference of water breakthrough time in the grid with 100 cells and 150 cells is less than 1% but the simulation time is a lot longer for the 150 cells option. Therefore, the model option with 100 grid cells in k-direction is chosen for further simulations. The water breakthrough times are summarized in Table 3.10.

Table 3.10 – Water breakthrough times for the different grid options, small diameter core

Number of blocks [k]	Block size k [cm]	Water BT [hrs]
10	3.048	11.82
50	0.6096	13.03
100	0.3048	13.18
150	0.2032	13.23

The 3D representation of the small core sample can be seen in Figure 3.7.

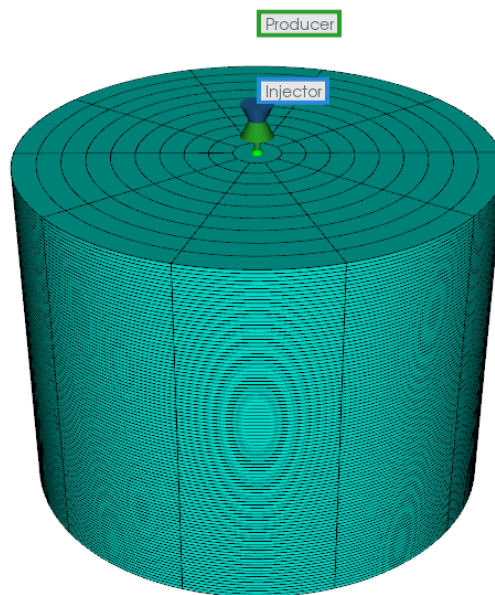


Figure 3.7 – 3D representation of the small diameter core sample in cylindrical coordinates.

3.5 Field Scale Setup

For the field scale simulation, a five-spot vertical-well pattern with a water injection of 400 bbl/day ($63.6 \text{ m}^3/\text{day}$) was chosen. The temperature of the injected water was $2 \text{ }^\circ\text{C}$ and the production well constraint was the reservoir pressure, same as in the coreflood parameters, of 7190 kPa. The area of the field was assumed to be 4 acres. The grid was chosen to show a local refinement around the wellbore. This resulted in a grid block size of 1.82 m for the refined blocks and 9.09 m for the other blocks with a thickness of 5 m, respectively. The reservoir depth was 650 m with a net pay thickness of 60 m. The vertical permeability (k -direction) was set to 10% of the horizontal permeability. The simulation duration was considered to be three years.

A 3D representation of the field scale model is shown in Figure 3.8.

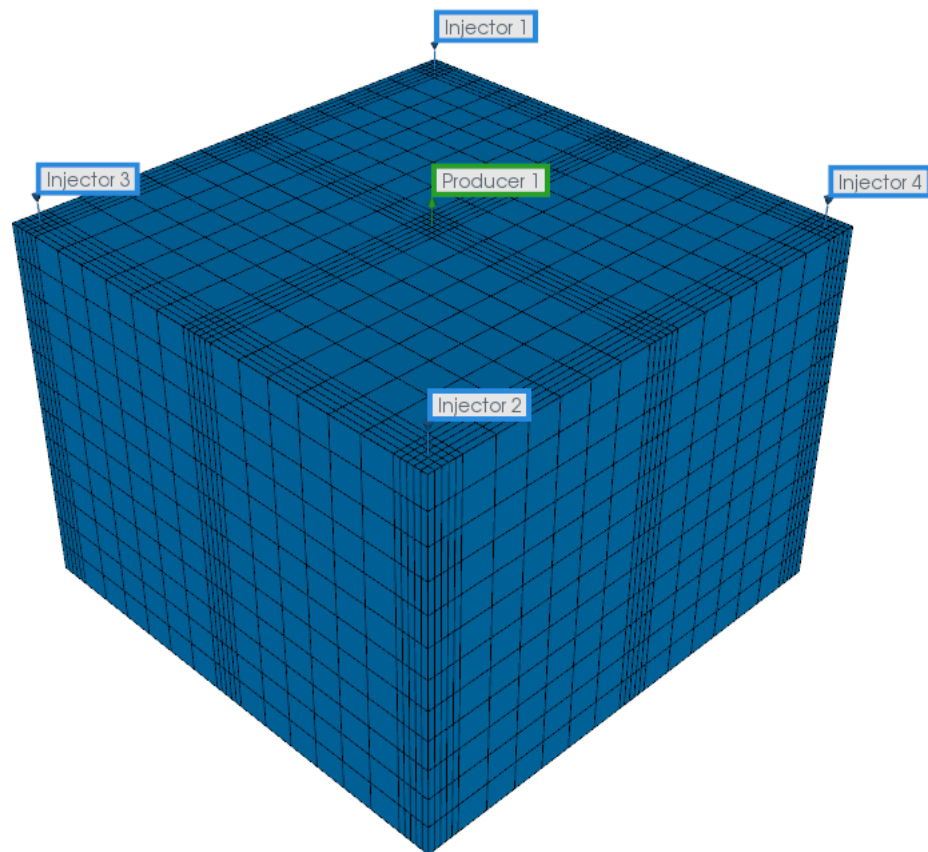


Figure 3.8 – 3D representation of the field scale model.

Chapter 4

Results and Discussion

This chapter presents the results of the experimental study, the analytical waterflooding solution and the numerical simulations followed by discussion.

4.1 Experimental Coreflood Results

This section summarizes relevant results that were obtained from the experimental study by Bianca Geranutti in her master's thesis in 2020.

4.1.1 Large Diameter Core Sample

The location of the waterfront during injection in the core has been determined by compressional wave velocity measurements. Thereby, a travel time difference of the injected water between the previous injection step and the current one tells where the waterfront is in the core. Figure 4.1 shows this difference between the 10 °C injection step and the 8 °C injection step at transducer location P4. This means that the waterfront has traveled from the bottom of the core to four inches measured from the top of the core after 3.5 hours of injection, resulting in 6.5 inches of travel length.

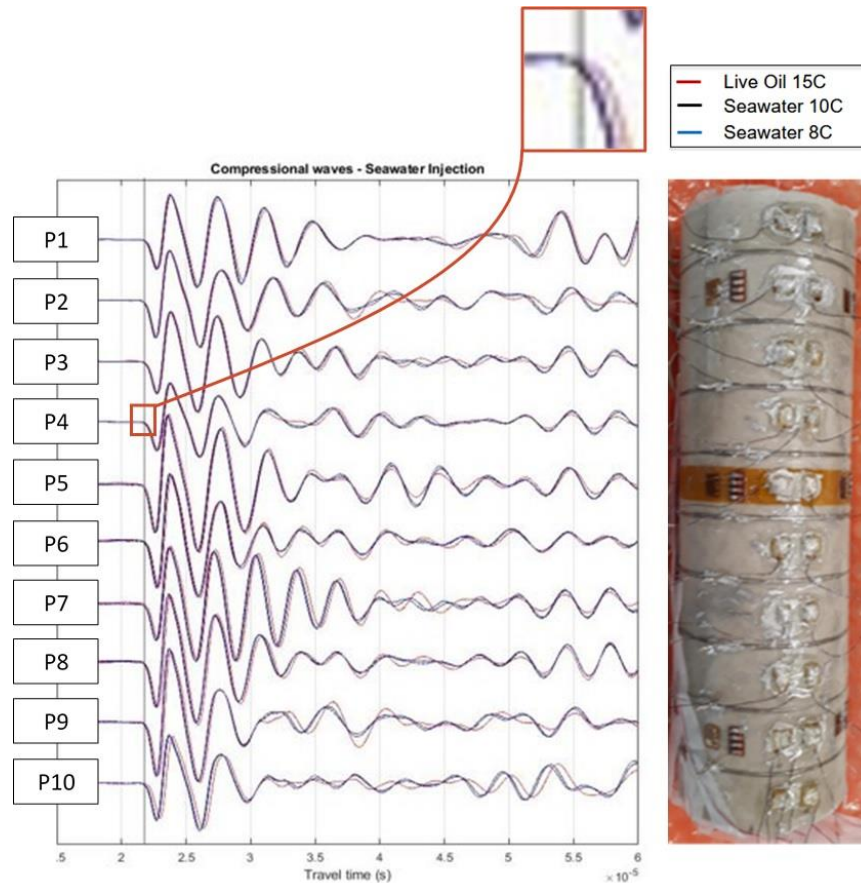


Figure 4.1 – Waterfront location determination using compressional wave velocities (Geranutti 2020).

4.1.2 Small Diameter Core Sample

As mentioned in Chapter 1, both, the large diameter core sample, and the small diameter core sample were subject to a cooling temperature ramp in the experiments. Pressure differential measurements between the bottom and the top of the core have been performed on the small diameter core sample during this temperature ramp which gave indirect information about significant formation of hydrates at 7 °C as the pressure drop at this point is very much increased. Figure 4.2 shows this pressure differential increase during the cooling of the core and the injected water.

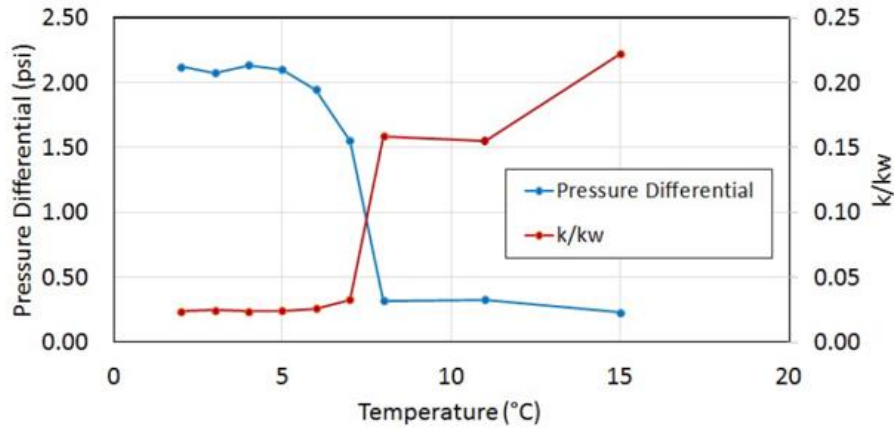


Figure 4.2 – Pressure differential in the temperature ramp of the experiments (Geranutti 2020).

After the cooling to the final temperature step of 2 °C, an injection ramp was performed keeping the temperature constant. The variation of the injection rate showed different pressure drops as can be seen in Figure 4.3a. Furthermore, an injection ramp at a constant temperature of 15 °C was performed (Figure 4.3b) to compare the pressure drop when no hydrates are expected with the pressure drop at 2 °C where hydrates are assumed.

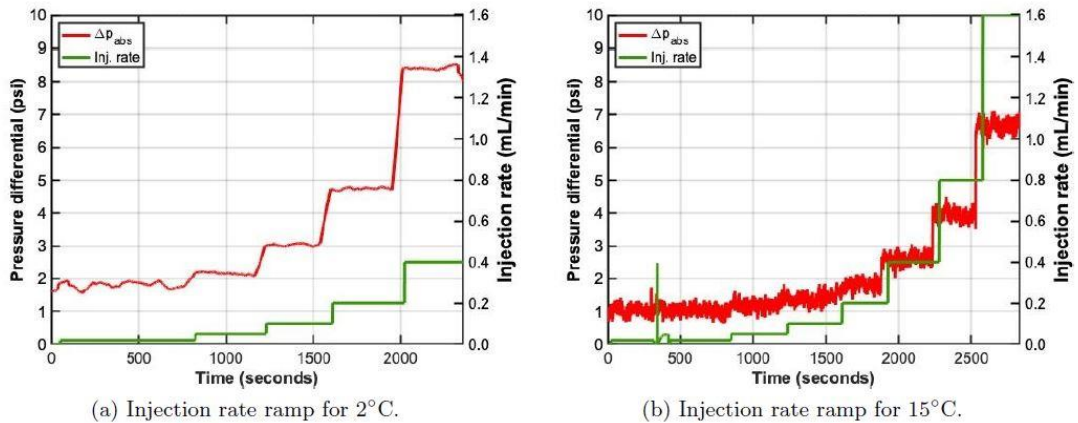


Figure 4.3 – Injection ramp at (a) 2 °C and (b) 15 °C (Geranutti 2020).

The injection scenario for the injection ramp at 2 °C are summarized in Table 4.1 and at 15 °C in Table 4.2.

Table 4.1 – Injection Ramp at 2 °C

Time [s]	Injection rate [cm ³ /min]
825	0.02
405	0.05
378	0.1
413	0.2
338	0.4

Table 4.2 – Injection Ramp at 15 °C

Time [s]	Injection rate [cm ³ /min]
850	0.02
389	0.05
374	0.1
310	0.2
357	0.4
298	0.8
257	1.6

4.2 Analytical Waterflooding Solution Results

To compare the experimental results with computed values, the analytical solution of the Buckley-Leverett flow equation is described below. The input parameters are listed in Table 4.3.

Table 4.3 – Input parameters for the analytical Buckley-Leverett solution

Parameter	Value
Porosity [-]	0.26
Area [in ²]	7.0686
Endpoint relative permeability of water [-]	0.44
Endpoint relative permeability of oil [-]	0.94
Connate water saturation [-]	0.1
Residual oil saturation [-]	0.2
n_w [-]	2
n_o [-]	2
Water viscosity [cp]	1.05878
Oil viscosity [cp]	2.49269
Injection rate [cm ³ /min]	0.2

In the Buckley-Leverett solution, first, the relative permeability curves of the system are calculated using modified Brooks-Corey model. The relative permeability of water is given by:

$$k_{rw} = k_{rw,max} \left(\frac{S_w - S_{wc}}{1 - S_w - S_{or}} \right)^{n_w} \quad (4.1)$$

where $k_{rw,max}$ is the end-point relative permeability of water, S_w is the water saturation, S_{wc} is the connate water saturation, S_{or} is the residual oil saturation, and n_w is the modified Brooks-Corey exponent for water.

The relative permeability of oil is given by:

$$k_{ro} = k_{ro,max} \left(\frac{1 - S_w - S_{or}}{1 - S_{wc} - S_{or}} \right)^{n_o} \quad (4.2)$$

where $k_{ro,max}$ is the end-point relative permeability of oil, S_w is the water saturation, S_{wc} is the connate water saturation, S_{or} is the residual oil saturation, and n_o is the modified Brooks-Corey exponent for oil.

The relative permeability curves are shown in Figure 4.4.

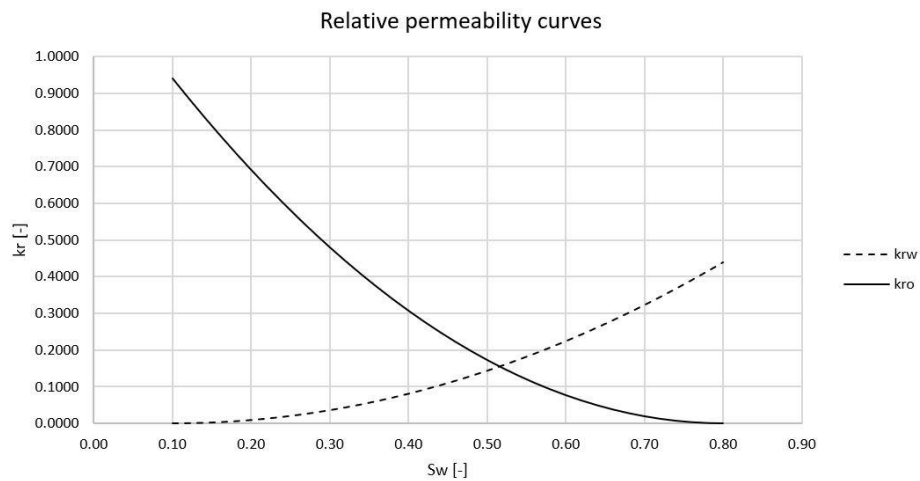


Figure 4.4 – Relative permeability curves of oil and water.

With these relative permeability values, the fractional flow of water is calculated by:

$$f_w = \frac{1}{1 + \frac{k_{ro}\mu_w}{k_{rw}\mu_o}} \quad (4.3)$$

where k_{ro} is the relative permeability of oil, μ_w is the viscosity of water, k_{rw} is the relative permeability of water, and μ_o is the viscosity of oil.

The derivative of the fractional flow of water with respect to the water saturation is described by:

$$\frac{df_w}{dS_w} = \frac{f_{wi+1} - f_{wi}}{S_{wi+1} - S_{wi}} \quad (4.4)$$

where f_{wi+1} is the fractional flow of water at location $i+1$, f_{wi} is the fractional flow of water at location i , S_{wi+1} is the water saturation at location $i+1$ and S_{wi} is the water saturation at location i .

Both, the fractional flow of water and its derivative with respect to the water saturation are shown in Figure 4.5.

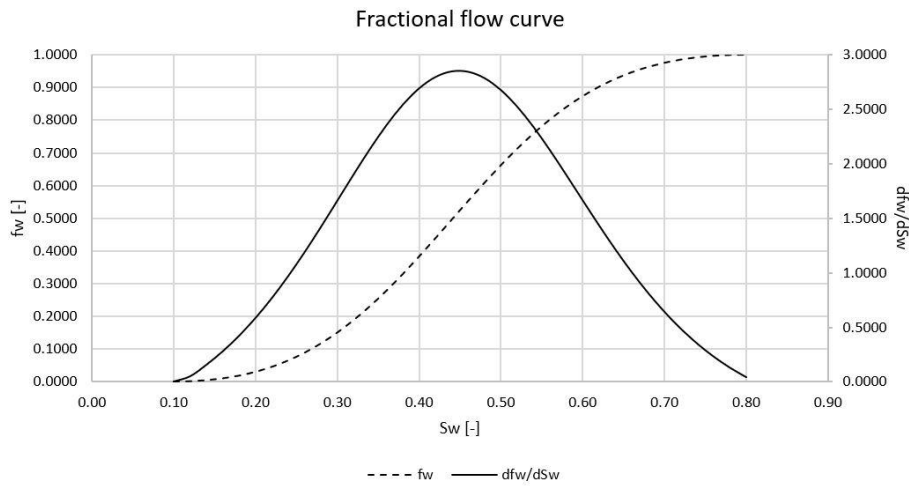


Figure 4.5 – Fractional flow curve of water.

Then, the location of the waterfront can be calculated as follows:

$$x = \frac{tq_t df_w}{A\phi dS_w} \quad (4.5)$$

where t is the time, q_t is the injection rate, A is the area, ϕ is the porosity, and $\frac{df_w}{dS_w}$ is the derivative of the fractional flow of water with respect to the water saturation.

To compare the location of the waterfront with the experimental results, the time is set to 3.5 hours. The water saturation profile is shown in Figure 4.6 and according to this analytical calculation of the Buckley-Leverett equation, the waterfront traveled 2.65 inches after 3.5 hours.

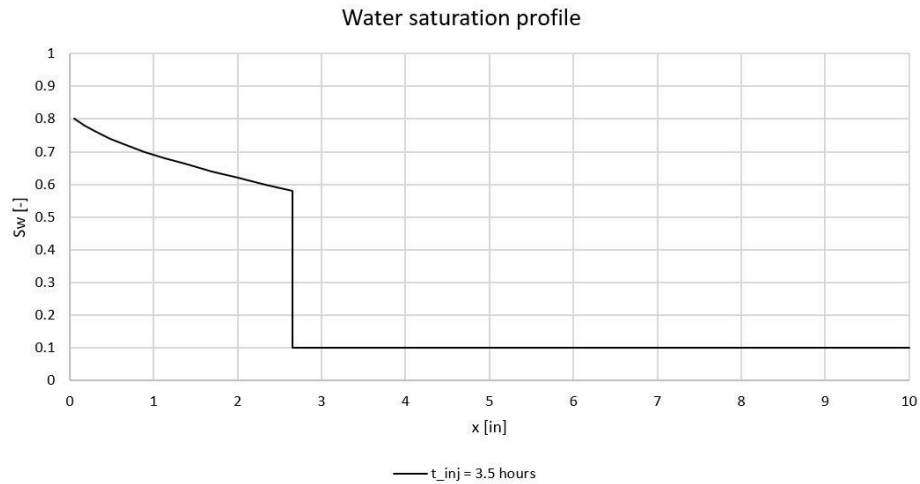


Figure 4.6 – Water saturation profile after 3.5 hours of injection.

4.3 Numerical Coreflood Simulation Results

This section gives the results of the numerical simulations with the Cartesian grid and the radial grid approach on the coreflooding scale.

4.3.1 Cartesian Grid

In the numerical model setup using Cartesian coordinates, there is only one cell in each depth layer over the whole cross-sectional area of the core. This results in a uniform waterfront propagation in z-direction from the bottom of the core, where the injection well is perforated, to the top of the core, where the production well is perforated. Figure 4.7 shows the waterfront location after 3.5 hours of injection to be at 2.6 inches measured from the bottom of the core.

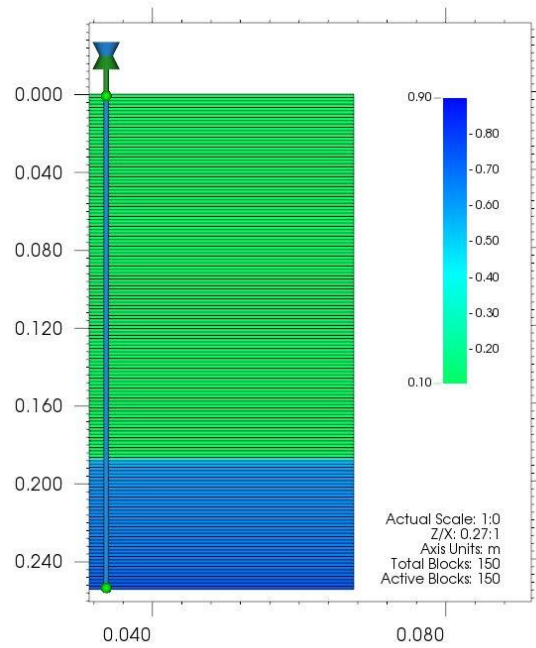


Figure 4.7 – Waterfront location after 3.5 hours of injection in the Cartesian model.

4.3.2 Radial Grid – Large Diameter Core Sample

In the numerical model using cylindrical coordinates, water is injected in the center cell and does not uniformly propagate throughout the core, but forms a pattern shown in Figure 4.8.

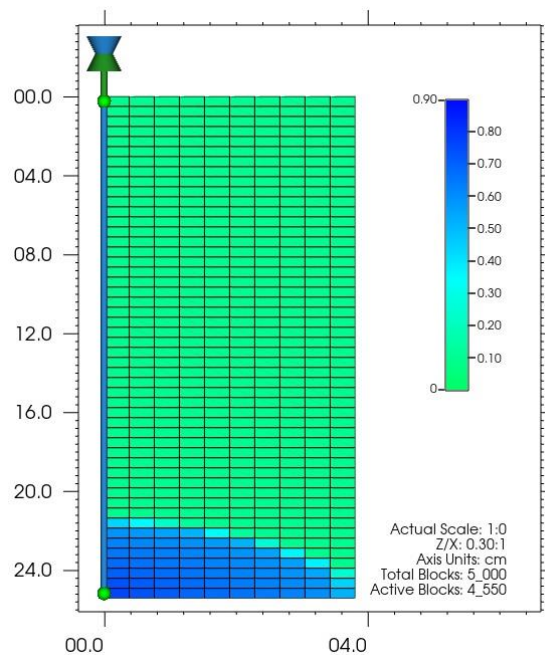


Figure 4.8 - Waterfront location after 1 hour of injection in the large core radial model.

After 3.5 hours of injection without accounting for the spontaneous imbibition effect, the waterfront reaches a location of 3.4 inches as can be seen in Figure 4.9.

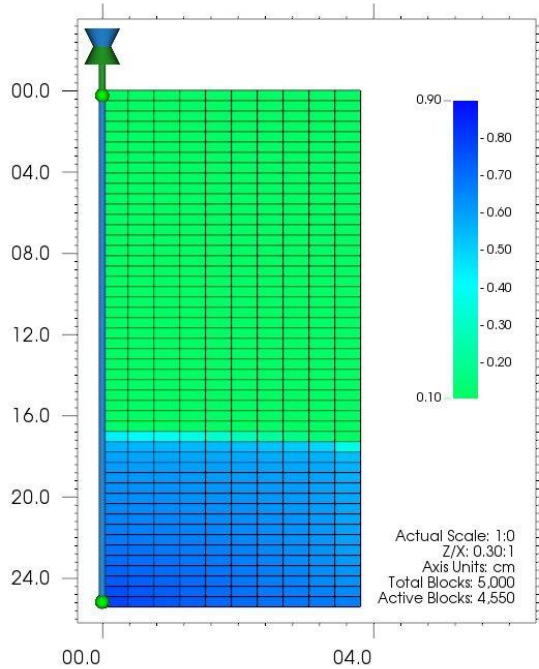


Figure 4.9 – Waterfront location after 3.5 hours of injection in the large core radial model.

To match the experimental observation of the waterfront location, data of a fine-tuned capillary pressure curve which is in the range observed in the Wisting field has been implemented. Figure 4.10 shows the capillary pressure curve and Figure 4.11 shows the waterfront location after 3.5 hours of injection accounting for the capillary pressure curve to be at 6.5 inches, which matches the experiments.

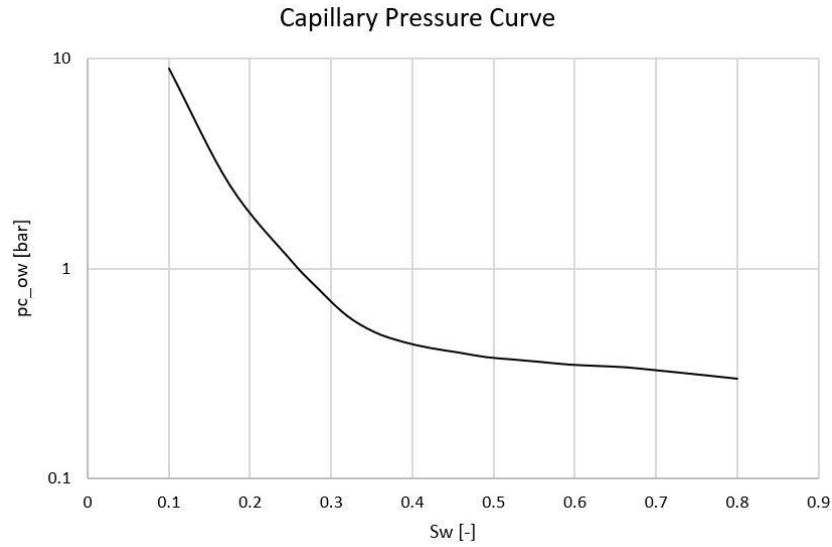


Figure 4.10 – Capillary Pressure Curve.

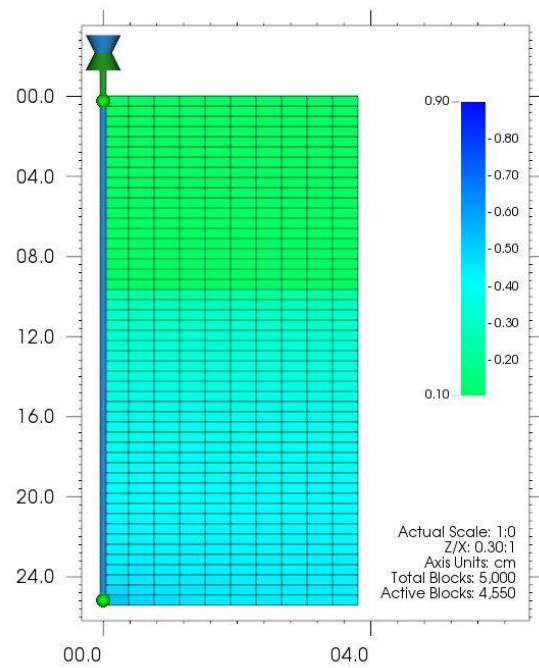
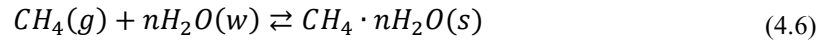


Figure 4.11 – Waterfront location after 3.5 hours of injection in the large core radial model including the capillary pressure effect.

After this base model, the formation of hydrates has been investigated. It was assumed, that only the C1 component in the oil, which represents methane, forms hydrates. The chemical reaction for this process is described by:



where $CH_4(g)$ is methane in gaseous phase, n is the stoichiometric coefficient, $H_2O(w)$ is water, and $CH_4 \cdot nH_2O(s)$ is gas hydrate in the solid phase.

On average, one mole of hydrate consists of 46 water molecules and eight encaged methane molecules. This leads to a value for the stoichiometric coefficient n of 5.75.

The hydrate formation reaction describes the change of hydrate concentration over time and is given by (Uddin et al. 2008):

$$\frac{dc_{hyd}}{dt} = A(\phi S_w \rho_w)(\phi S_{hyd} \rho_{hyd}) \left(\frac{1}{K} - 1 \right) \exp \frac{-\Delta E}{RT} \quad (4.7)$$

where A is the frequency factor, ϕ is the porosity, S_w is the water saturation, ρ_w is the density of water, S_h is the hydrate saturation, ρ_{hyd} is the density of hydrates, K is the rate between pressure and hydrate equilibrium pressure, ΔE is the activation energy, R is the universal constant, and T is the temperature.

The hydrate equilibrium pressure is obtained from PVT measurements at certain temperatures for different fluid samples. Figure 4.12 shows the resulting hydrate equilibrium curves for formation water, seawater, and freshwater, respectively.

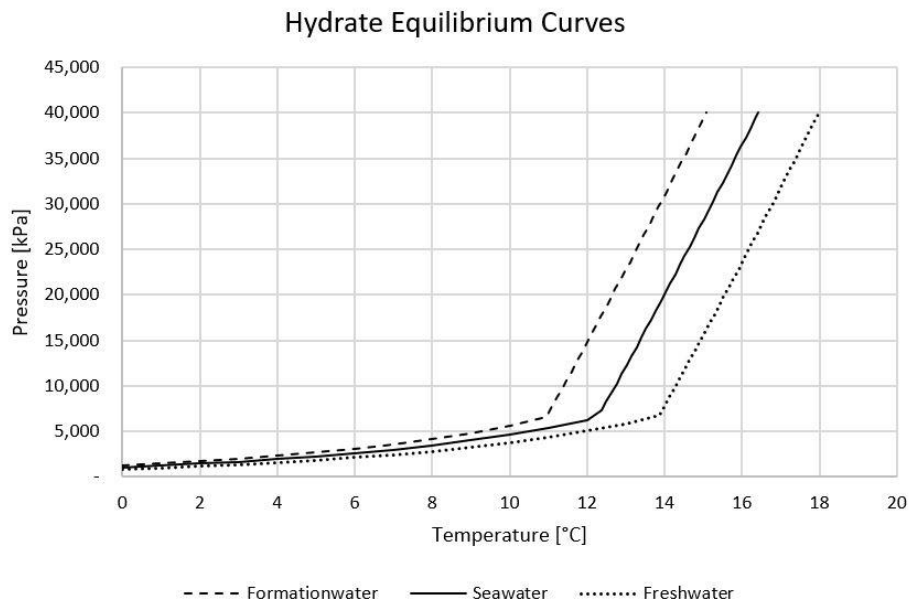


Figure 4.12 – Hydrate equilibrium curves for formation water, seawater, and freshwater.

The rate between pressure and hydrate equilibrium pressure, or K-values, represents the deviation from hydrate equilibrium conditions, and it is used to estimate the driving force of whether hydrates are formed or dissociated. The K-values are represented by the following exponential relation for different pressure and temperature conditions:

$$K = \frac{k1}{P} \exp \frac{k2}{(T - k3)} \quad (4.8)$$

where P is the pressure, T is the temperature, and k1, k2, and k3 are coefficients fitted to phase equilibrium data.

If K is larger than one, the system is outside of the hydrate stability region, leading to a negative hydrate formation equation, which means that hydrates will dissociate. If K is lower than one, the system will be inside the hydrate formation region and hydrates will form.

The fitting parameters need to be determined in order for the simulation software to compute when and how much hydrates will be formed or dissociated.

These parameters were calibrated using regression analysis for hydrate equilibrium conditions at different water salinities (i.e., seawater and formation water). The regression analysis has been performed with MATLAB to fit a surface dictated by different hydrate equilibrium conditions in terms of pressure and temperature. The resulting surface for seawater is shown in Figure 4.13 and the resulting surface for formation water is shown in Figure 4.14.

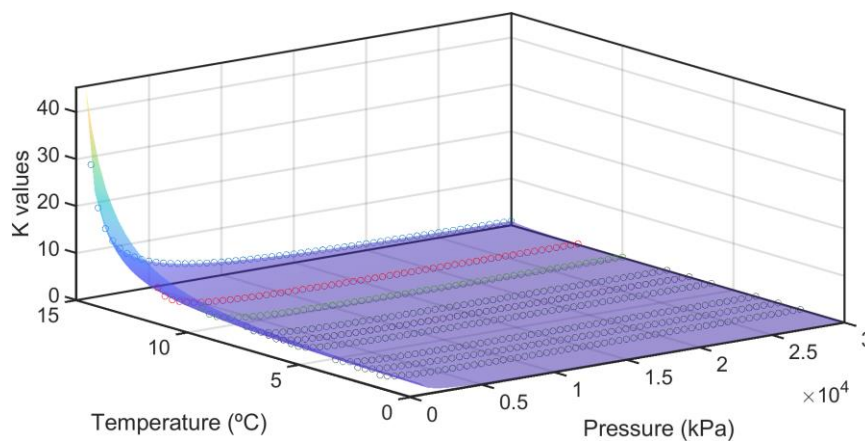


Figure 4.13 – Surface for seawater.

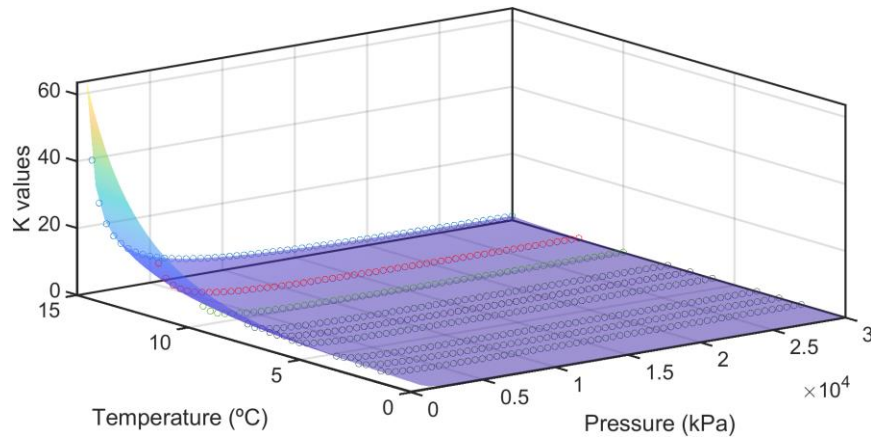


Figure 4.14 – Surface for formation water.

The K-values correlation coefficients with their corresponding coefficient of determination, R^2 , indicating the goodness of the fit are summarized in Table 4.4.

Table 4.4 – Fitting parameters k_1 , k_2 , k_3

	k1	k2	k3	R² [%]
Formation water	10.19	-160.2	34.37	99.66
Seawater	706.5	-17.29	19.7	99.88

Further input parameters for the hydrate formation reaction are summarized in Table 4.5.

Table 4.5 – Hydrate reaction parameters

Parameter	Value
Activation energy [kJ/gmol]	89.66
Reaction frequency factor [-]	$1.097058 * 10^{13}$
Formation enthalpy [kJ/gmol]	-51.858
Dissociation enthalpy [kJ/gmol]	51.858

To model the hydrate formation following the temperature ramp, separate simulation files have been created. Each simulation file is initialized with the resulting conditions from the previous temperature step simulation results.

This resulted in the hydrate concentration distribution along the core for each temperature step shown in Figure 4.15.

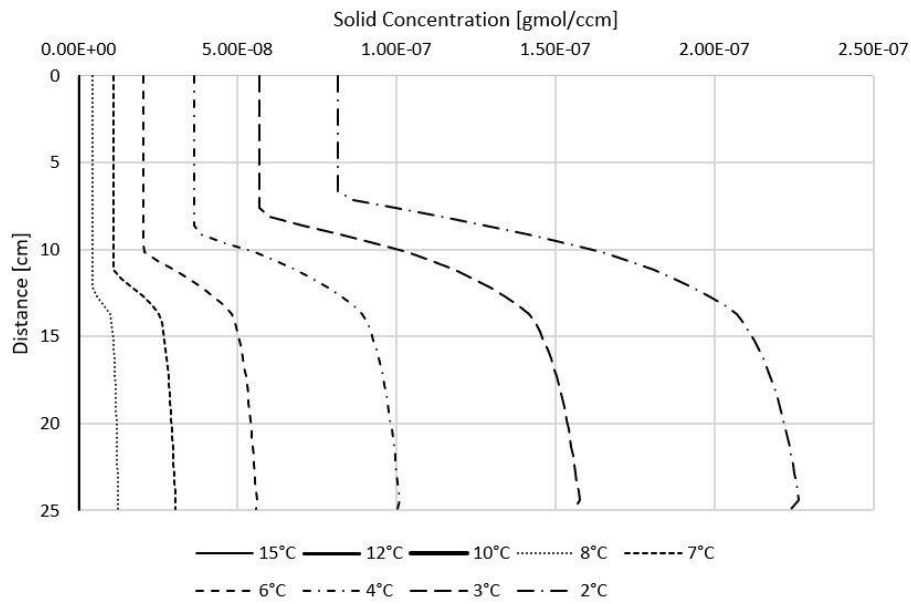


Figure 4.15 – Hydrate concentration along the core for every temperature step, large diameter core.

The hydrate concentration was converted to hydrate saturation by:

$$S_{hyd} = \frac{c_{hyd} * M_{hyd}}{\rho_{hyd} * \phi} \quad (4.9)$$

where c_{hyd} is the hydrate concentration, M_{hyd} is the molecular weight of hydrates, ρ_{hyd} is the density of hydrates and ϕ is the porosity.

Table 4.6 summarizes the parameter values for this calculation and Figure 4.16 shows the distribution of hydrate saturation along the core.

Table 4.6 – Parameters for the conversion of hydrate concentration to hydrate saturation

Parameter	Value
M_{hyd} [g/gmol]	119.63
ρ_{hyd} [g/ cm ³]	0.9

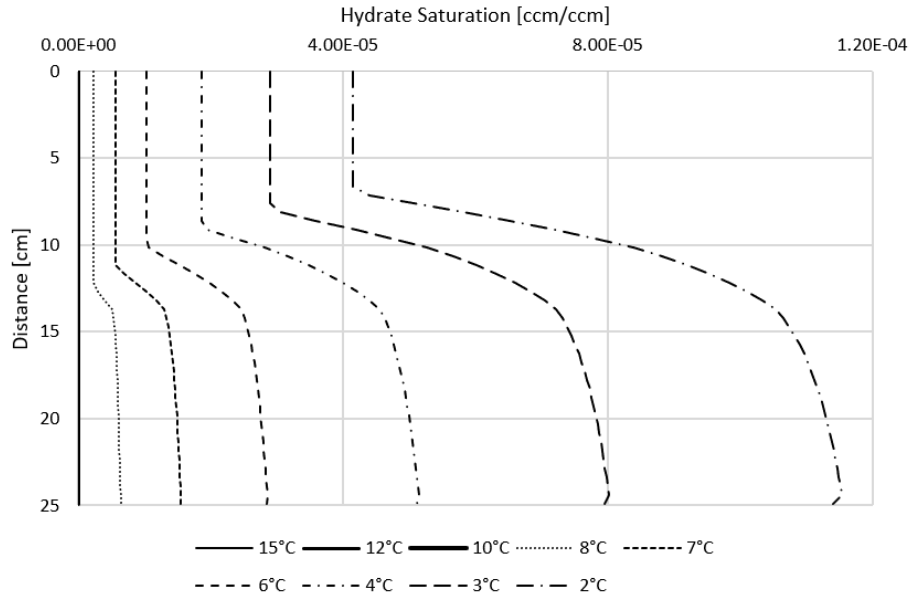


Figure 4.16 – Hydrate saturation along the core for every temperature step, large diameter core.

4.3.3 Radial Grid – Small Diameter Core Sample

The numerical model representing the small diameter core sample was used to compare the effects of hydrate formation throughout the core with the pressure differential measurements in the experiments.

Following the same temperature ramp for the small diameter core sample as in the experiments, the numerical model resulted in a pressure differential along the core shown in Figure 4.17.

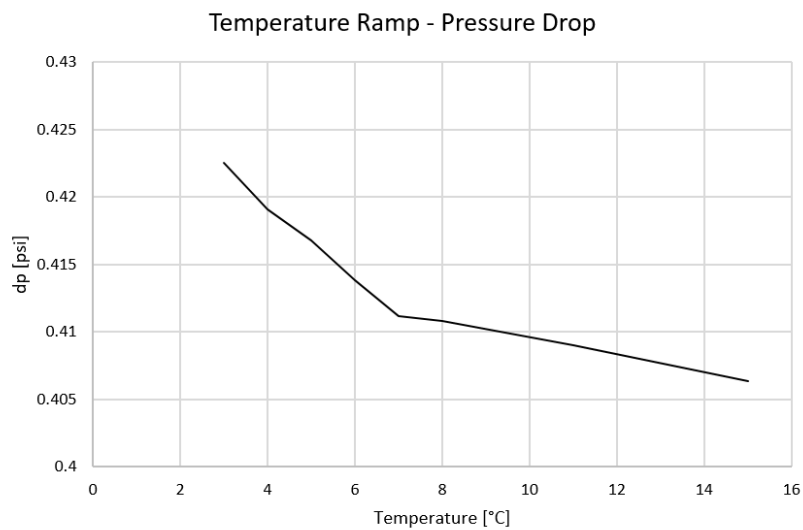


Figure 4.17 – Predicted pressure differential for the temperature ramp, small diameter core.

For the injection ramp at the final temperature step with a constant 2 °C temperature, the pressure drop along the core is shown in Figure 4.18.

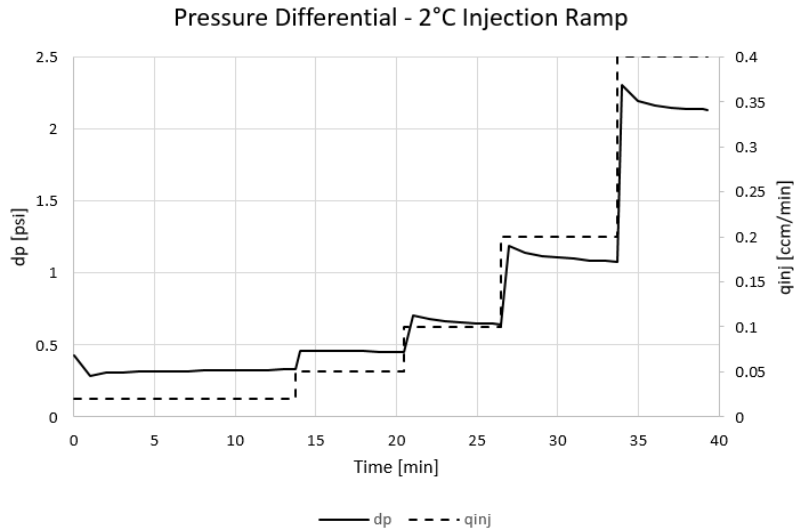


Figure 4.18 – Pressure differential for the injection ramp at 2 °C with seawater injection, small diameter core.

The pressure differential along the core for the injection ramp at a constant temperature of 15 °C where no hydrates were expected is shown in Figure 4.19.

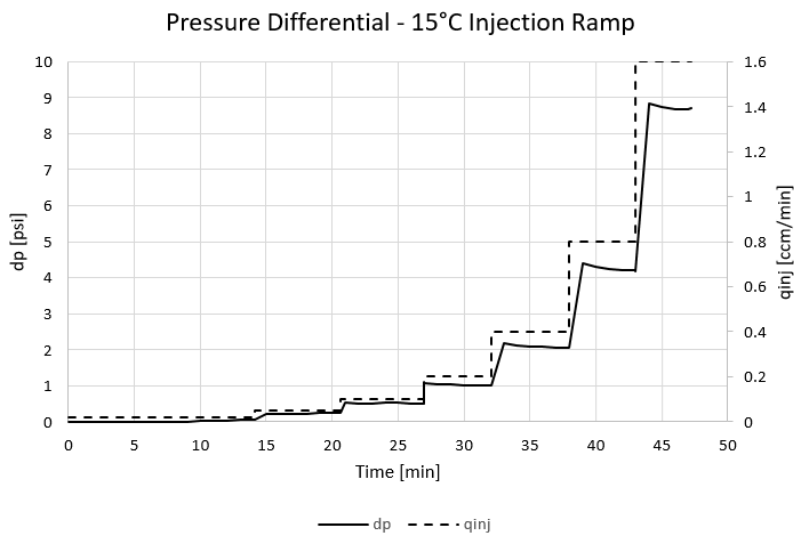


Figure 4.19 – Pressure differential for the injection ramp at 15 °C with seawater injection, small diameter core.

The hydrate saturation distribution along the core for all the temperature steps is given in Figure 4.20.

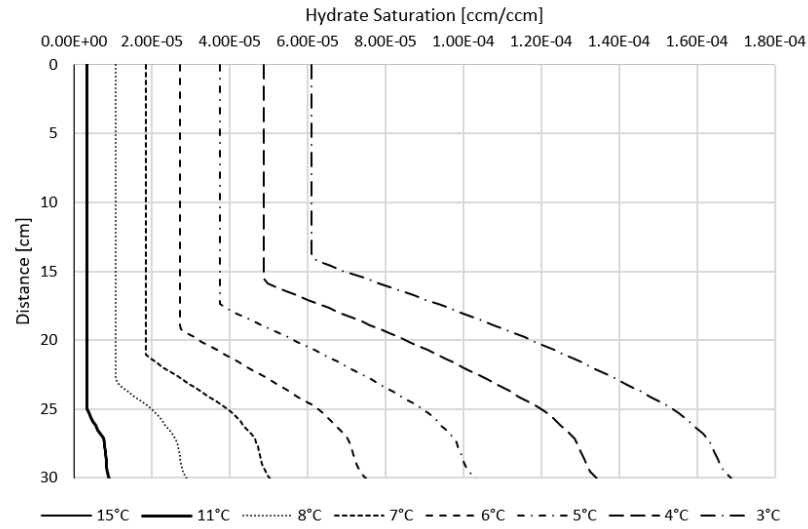


Figure 4.20 – Hydrate saturation along the core for every temperature step, small diameter core.

The permeability along the core, that is calculated by the Kozeny model, with all the temperature steps is shown in Figure 4.21.

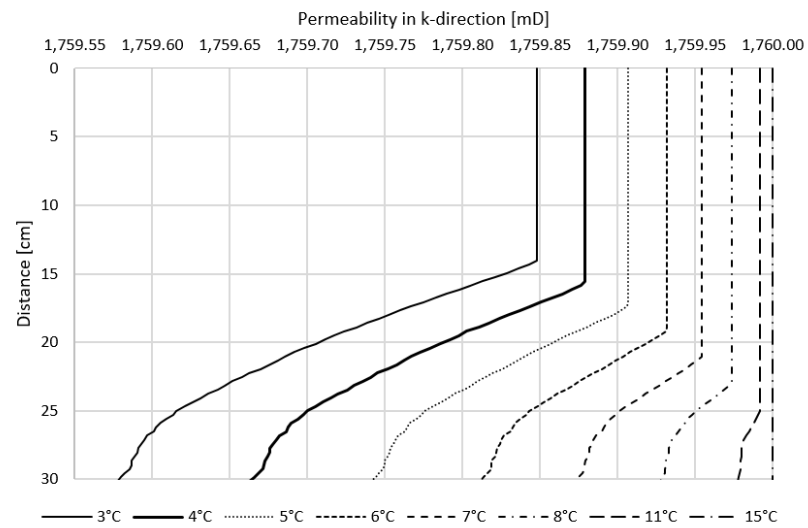


Figure 4.21 – Permeability in k-direction along the core for every temperature step, small diameter core.

As the pressure differential observed in the experiments does not match the values from the numerical computation and the hydrate saturation is very low, it is assumed that in reality more hydrates were formed. To verify this assumption, the simulations were performed with an increased value of the hydrate frequency factor.

Increasing the hydrate reaction frequency factor by two orders of magnitude gives a hydrate saturation increase also by two orders of magnitude. The hydrate saturation profile after the 3 °C temperature step for comparison is shown in Figure 4.22.

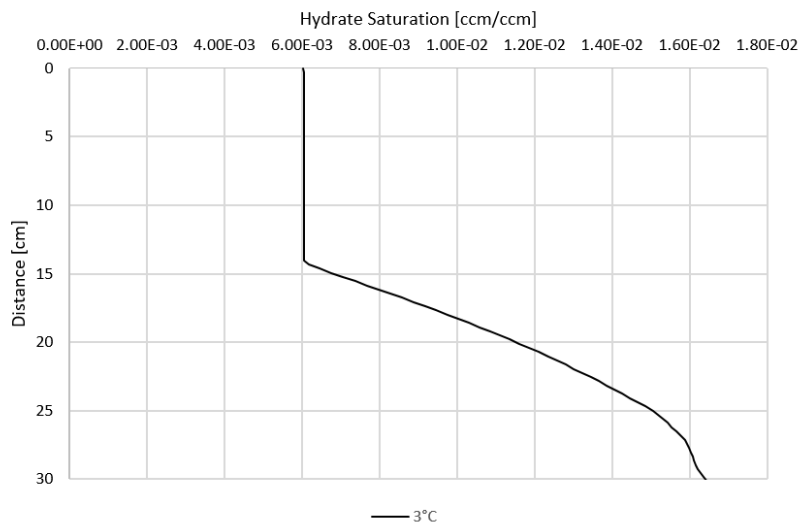


Figure 4.22 – Hydrate saturation along the core after the 3 °C temperature step with an increase by two orders of magnitude of the reaction frequency factor, small diameter core.

The permeability along the core in the case of an increased hydrate reaction frequency factor by two orders of magnitude is shown in Figure 4.23.

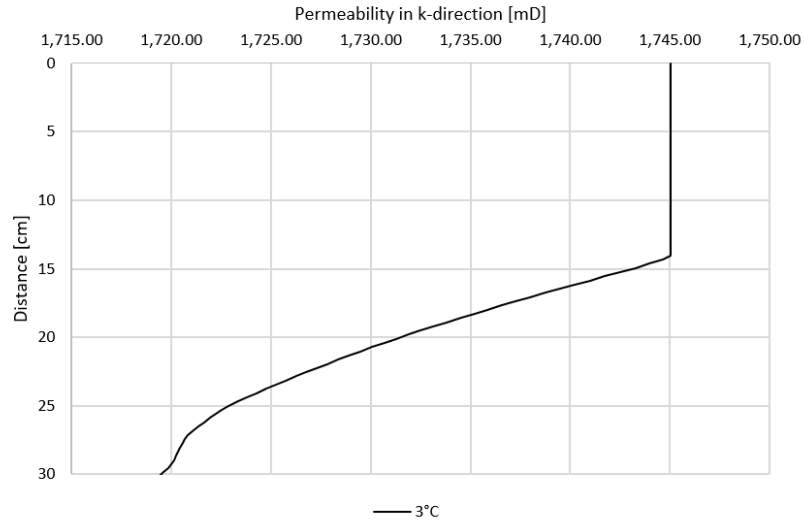


Figure 4.23 – Permeability in k-direction along the core after the 3 °C temperature step with an increase by two orders of magnitude of the reaction frequency factor, small diameter core.

Another assumed possibility to form more hydrates is to keep the core within the hydrate formation region for a specific amount of time. Keeping the core for 24 hours after the temperature ramp at a constant temperature of 2 °C without injecting water or producing oil, shows an increase of the amount of hydrates that form by one order of magnitude (Figure 4.24).

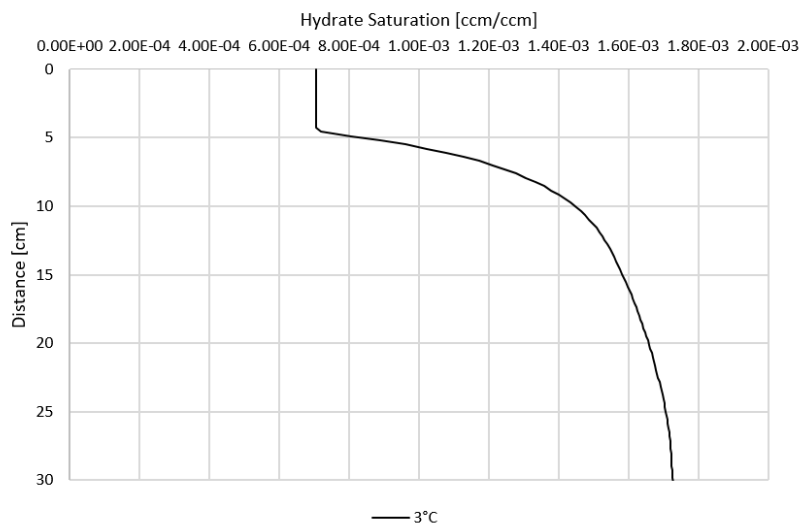


Figure 4.24 – Hydrate saturation along the core after the 3 °C temperature step and keeping the core at constant 2 °C for 24 hours without injection or production, small diameter core.

The artificial increase of the hydrate formation frequency factor to force the simulations to a higher hydrate formation does not resemble reality. It is seen that hydrates are continuously forming with time even without water injection.

In the experiments, the core was cooled after each temperature step overnight. Therefore, also the simulations have been adjusted to reproduce that. Each simulation temperature step was kept at the specific temperature without water injection or oil production for the time of 23.5 hours after the 30 min injection. The resulting hydrate saturation throughout the core can be seen in Figure 4.25.

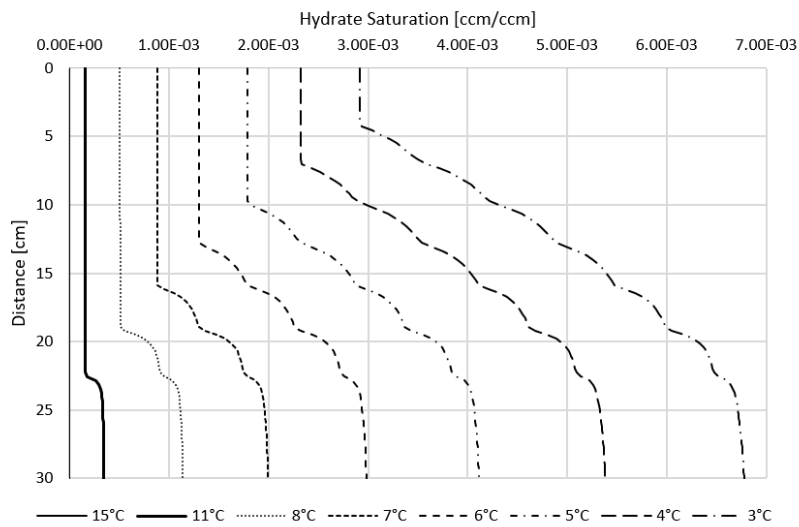


Figure 4.25 – Hydrate saturation along the core for each temperature step simulating 24 hours, small diameter core.

However, the higher hydrate saturation resulting from these experiments shows a similar pressure differential along the core shown in Figure 4.26.

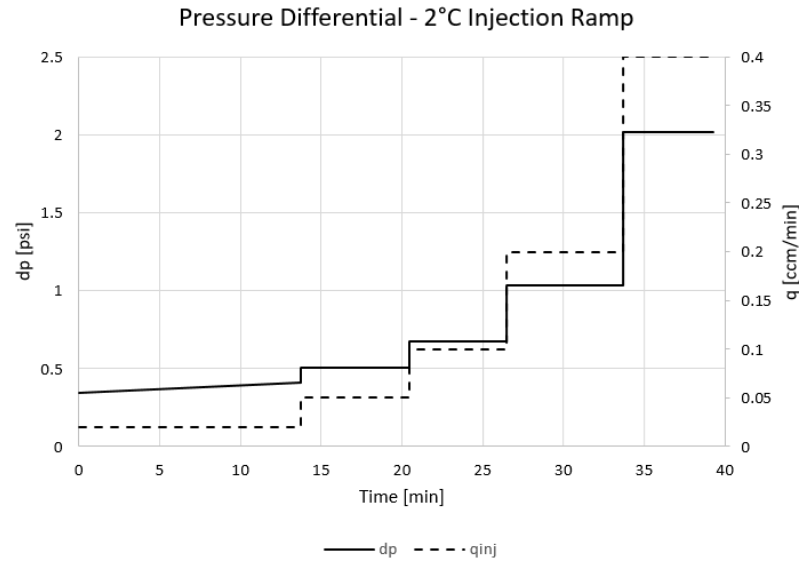


Figure 4.26 – Pressure differential for the injection ramp at 2 °C for the 24 hours simulations, small diameter core.

4.3.4 Field Scale Simulation Results

The results of the capillary pressure curve and the fitting parameters for the hydrate formation equation in the case of seawater injection from the coreflood simulations have been implemented in the field scale model simulating hydrate formation and no hydrate formation.

This leads to water production versus time shown in Figure 4.27.

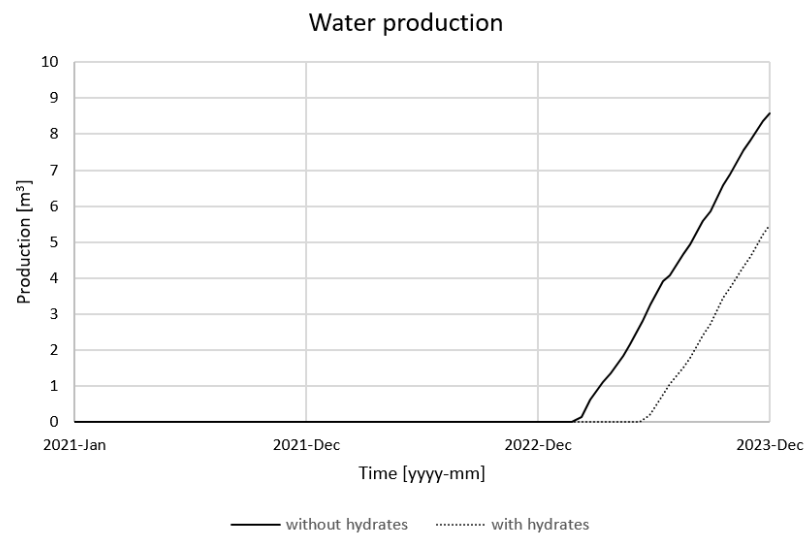


Figure 4.27 – Water production in the field scale model.

In the case of no hydrate formation, seawater with a temperature of 15 °C, which is outside the hydrate forming region, was injected and in the case of hydrate formation, seawater with 2 °C was injected.

The difference in the two models can also be seen in the bottomhole pressure of the injectors. In the case where hydrates form around the wellbore, the bottomhole pressure is higher than in the case where no hydrates are present (Figure 4.28).

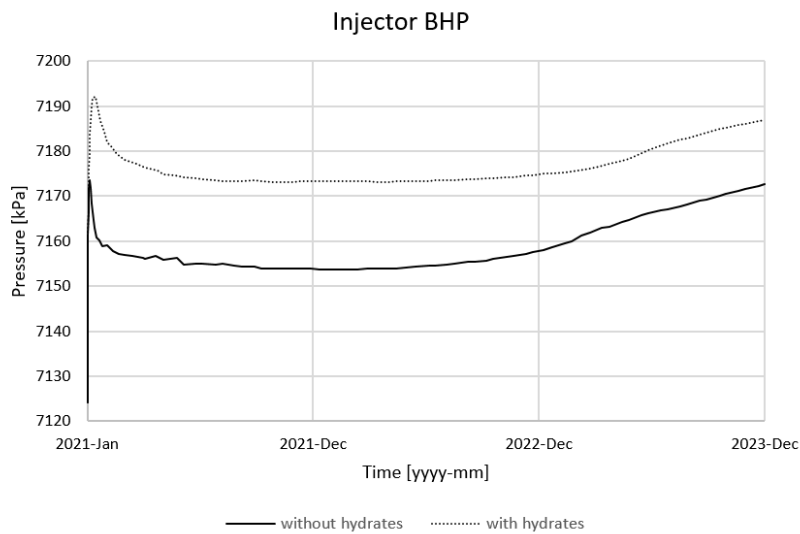


Figure 4.28 – Bottomhole pressure of the injector wells.

The hydrate concentration distribution in the areal view after three years of cold water injection is shown in Figure 4.29 and the solid concentration in the vertical view can be seen in Figure 4.30.

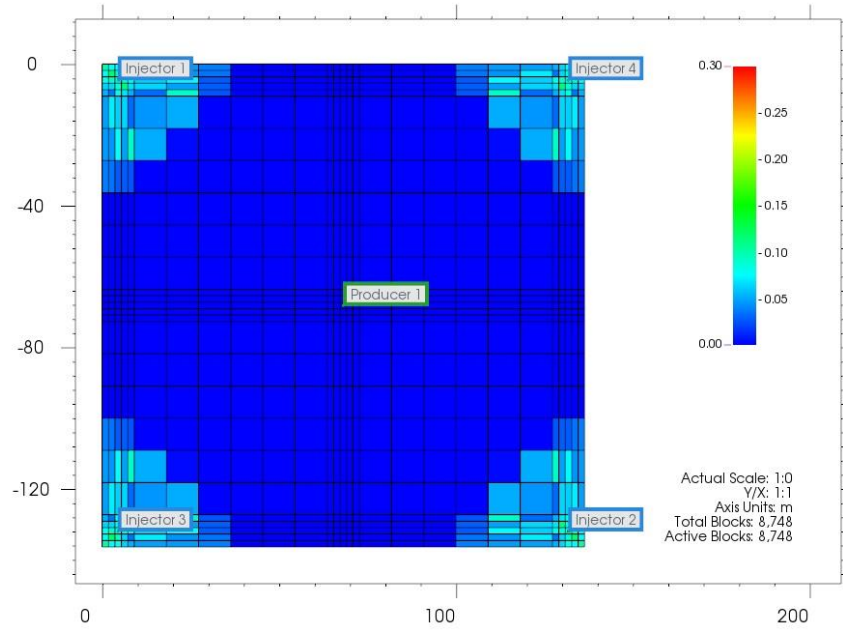


Figure 4.29 – Solid concentration in the areal view after three years of injection.

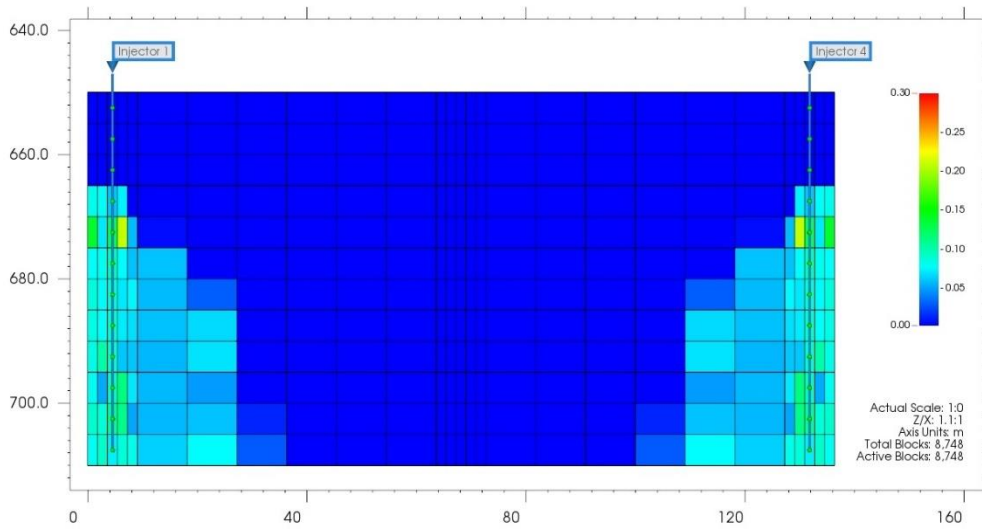


Figure 4.30 – Solid concentration in the vertical view after three years of injection.

The solid concentration leads to a significant permeability reduction from 2750 md to as little as 700 md in some blocks. The areal distribution of the permeability after three years of injection can be seen in Figure 4.31 and the vertical distribution is shown in Figure 4.32.

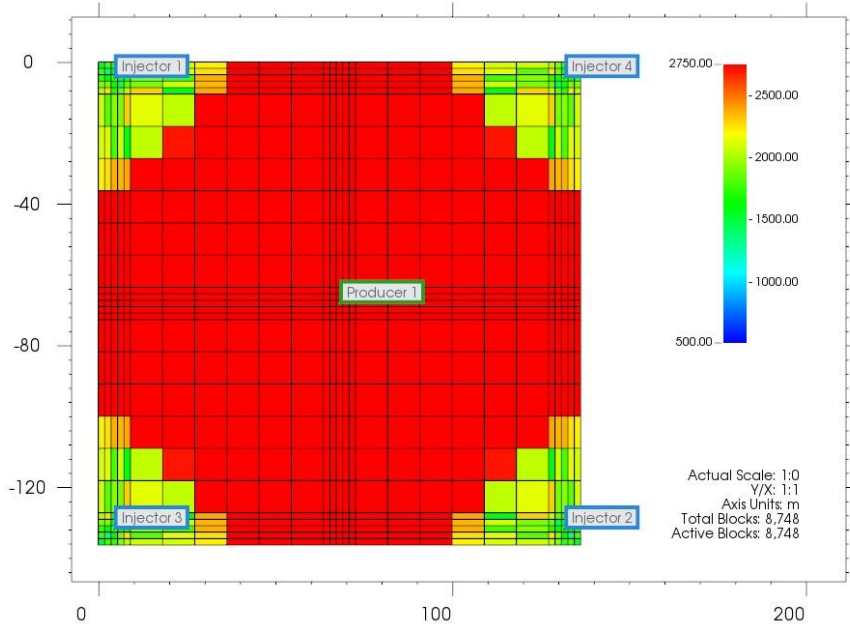


Figure 4.31 – Permeability distribution in the areal view after three years of injection.

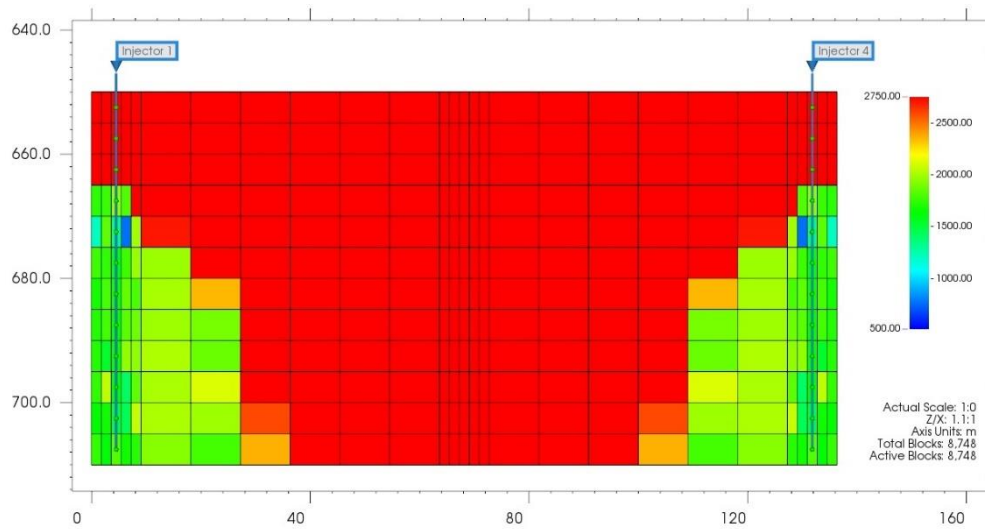


Figure 4.32 – Permeability distribution in the vertical view after three years of injection.

4.4 Discussion

The numerical models using cylindrical coordinates better resemble the physical geometry of the core samples used in the experimental setup than a numerical model in Cartesian coordinates.

Including capillary pressure data in the numerical models to account for the spontaneous imbibition effect besides the water injection, yields good base models that match the experimentally observed waterfront propagation.

Following the cooling temperature ramps from the non-hydrate forming region in the hydrate equilibrium curves to the hydrate forming region, did show the formation of hydrates as observed in the experiments.

Although the pressure between the injector and the producer that should have given information about the number of hydrates that formed showed the same trend as observed in the experiments, it did not quantitatively match them.

Changing the reaction frequency factor in the hydrate formation equation yields an increase in hydrate saturation in the same order of magnitude as the frequency factor change.

Keeping the model at a constant temperature within the hydrate forming region for a longer time than just following one simulation after another in the temperature ramp also showed an increase in the number of hydrates that formed. This led to the 24 hours simulation models with 30 min of injection and 23.5 hours of constant temperature wait time without injection or production.

While the permeability reduction at a hydrate saturation of 0.067% is only 0.425 md, the increase of the hydrate reaction frequency factor that gives a hydrate saturation at the same spatial point of 6.5% yields a permeability reduction of 41 md. This observation leads to the conclusion that the increase of the hydrate reaction frequency factor leads to the increase of hydrates in the same order of magnitude, which also results in the decrease of permeability in the same order of magnitude.

The field scale simulation with seawater injection at a temperature of 15 °C does not form hydrates as the conditions are outside the hydrate forming region of the hydrate stability curve. This leads to an earlier water breakthrough and higher ultimate cumulative water production compared to the case of seawater injection at a temperature of 2 °C where hydrates are forming. However, the bottomhole pressure of the injector wells is higher in the case with hydrates as the near-wellbore zone is plugged by hydrates which represents a barrier to fluid flow. This also reflects in the permeability reduction which is significant in the blocks where the hydrate saturation is high.

Chapter 5

Conclusion

5.1 Summary

A base case model in cylindrical coordinates was established through the match of the waterfront location detected by acoustic measurements in the experiments of a large diameter core sample. The parameters used in this model including the fine-tuned capillary pressure data have been implemented in a small diameter core model showing different physical dimensions and in a field scale model as well.

The small diameter core model was further used to compare the pressure differential along the core from an injection ramp experiment with the computed ones by the model. The comparison of the pressure differential along the core at a constant temperature where hydrates were expected (2 °C) with that of a constant temperature where no hydrates were expected (15 °C) did not match the experiments. The numerical simulation model underestimates the effect of gas hydrate saturation on reservoir permeability. Analysis of the hydrate formation reaction showed that the amount of hydrates formed in the simulations increased by the same order of magnitude with the increase of the hydrate reaction frequency factor.

In the numerical simulations, once the system pressure and temperature conditions enter the hydrate forming region of the hydrate stability zone, hydrates will form with time even without water injection. The simulation models are based on thermodynamic equilibrium and do not consider the metastable conditions observed in the experiments, where hydrate formation was triggered after the system reached a thermal driving force for hydrate nucleation. This thermal driving force, or subcooling, is defined as the difference between the hydrate equilibrium temperature and the system temperature inside the hydrate stability zone. Therefore, the amount of hydrates that form in the simulations, that are associated with an increase in the pressure

drop across the core, can only be seen as qualitative and cannot be compared to the absolute amount of hydrates that formed during the experiments, which are inferred from the pressure drop measurements.

The approach of the experiments to vary reaction kinetics and transport kinetics at the same time makes it very difficult to reach an exact match of simulation with experiments. Therefore, a systematic approach of how to perform the experiments needs to be developed using the information gained from the simulations.

The field scale simulations show the effect of hydrates in the near wellbore region which is an increase in the bottomhole pressure and a permeability reduction due to the hydrates plugging the pore space of the reservoir. This also leads to a longer water breakthrough time.

5.2 Evaluation

The overall objectives of the thesis were met by creating numerical reservoir simulation models that are able to reproduce coreflood experiments, show the conditions under which gas hydrates form, and how these gas hydrates will influence the permeability in the cores as well as in a five-spot pattern waterflooding operation on the field scale. However, it could not exactly be determined why the computed pressure differential using hydrate reaction data from literature did not match the measurements in the experiments. Furthermore, due to time constraints for this thesis, the final task to probe a realistic hydrate distribution on the pore scale could not be finished, but the basic information for this is given in the next section, Future Work, to facilitate the continuation of this study.

5.3 Future Work

Suggested future work for improving the numerical models for gas hydrate formation in oil reservoirs consist of investigating the hydrate formation at the pore scale to probe a realistic distribution of the solid phase within the rock pore volume that explains acoustic and electrical measurements. This section presents the basics of pore scale modeling in form of a short literature review. Furthermore, a close investigation of why the numerical models are not able to capture the pressure differential measurements from the experiments, and which parameters most influence the hydrate concentration equation, should be done in form of uncertainty and sensitivity analyses. Therefore, the effect of hydrate saturation on the permeability reduction can be estimated from acoustic measurements in the experimental setup.

5.3.1 Pore Scale Modeling

The processes and the arrangement of fluids within the reservoir depend on the microstructure of pores within the rocks (Herring, Robins, and Sheppard 2019). Especially, the prediction of multiphase flow behavior is very challenging, as often a complex wettability distribution and pore geometry are shown (Masalmeh et al. 2015).

It is almost impossible to get an exact distribution of the grains without extracting them because of various geological processes such as compaction and diagenesis that the reservoir underwent in the past (Ma et al. 2018).

The basis of modeling the inner structures of reservoir rocks on a pore scale is computer tomography (CT) images which are obtained through taking many X-ray pictures of the sample with a resolution of a few micrometers. Like in human bones, more dense parts in the rock such as the impermeable rock matrix appear lighter than for example the rock pore space and allows, therefore, to distinguish between them (Rassenfoss 2011). A 2D slice of a high-resolution micro CT scan of a Berea sandstone sample can be seen in Figure 5.1. The pore space in this figure is highlighted in dark colors, and denser material, such as grains, clay material, and the matrix appear in lighter colors.

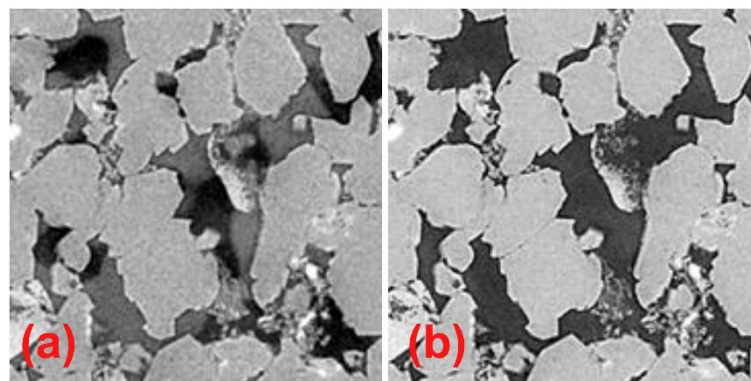


Figure 5.1 – Micro CT slice of a sandstone sample in (a) dry and (b) SIH state (Shabaninejad, Middleton, and Fogden 2018).

The steady increase in imaging and data processing capabilities throughout the last few years made it possible to develop algorithms describing the physics of multiphase flow behavior at the pore scale (Masalmeh et al. 2015).

Three major forces control the rock-fluid interactions including viscous, capillary, and gravity forces. The assumption of negligible gravity and capillary forces because of the diffusive

distribution of the fluids leads to the definition of the fluid flow behavior mainly by the wettability state influenced by relative permeabilities (Olofinnik 2019).

The presence of numerical errors such as discretization errors, iterative convergence errors, or round-off errors needs to be determined in order to ensure an accurate digital pore scale network that represents all the governing physics (Carpenter 2015).

A computationally very efficient method of multiphase flow modeling on the pore-scale to display local pressure and velocity distributions is the so-called Pore Network Model (PNM). However, PNM assumes simplified porous structures and physics. This is why it shows good results in a single capillary rise experiment and is able to predict the flow pattern in simple geometries but often fails in multiphase flow modeling of complex reservoir rocks in terms of pore size distribution and wettability (Yin et al. 2019).

Therefore, the Lattice Boltzmann method for two-phase flow, which is a numerical approach to solve a discrete form of the Boltzmann transport equation for the fluid particle distribution function is a better approach for multiphase flow modeling. It allows the display of isolated key features, such as the non-wetting phase distribution or the velocity field (Zhang et al. 2017; Landry et al. 2017). Figure 5.2 shows the Lattice Boltzmann evaluation of intrinsic permeability in a porous medium.

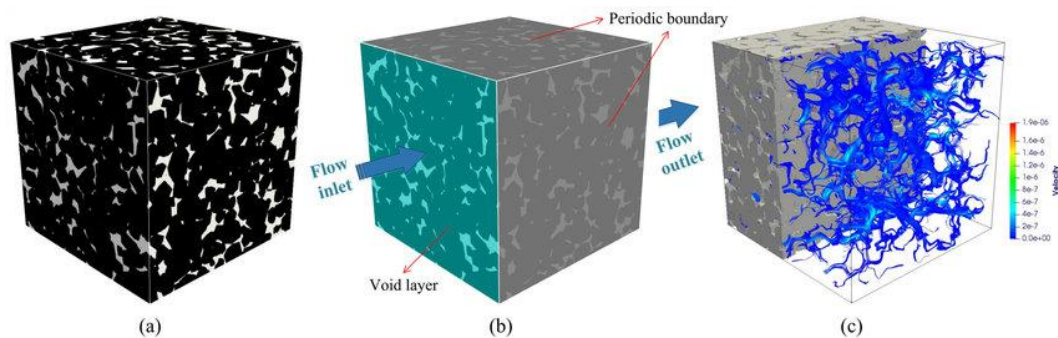


Figure 5.2 – Lattice Boltzmann evaluation of intrinsic permeability with (a) 3D digital image, (b) schematic fluid flow, and (c) steady state velocity field (Fu et al. 2020).

There exist several different types of the Lattice Boltzmann method but the first one and the most widely accepted one for multiphase flow modeling of immiscible displacement is the color gradient Lattice Boltzmann method. In this kind of numerical simulation, the displacing and displaced fluids are represented in blue and red, respectively. It accounts for the viscosity ratio effect and the interfacial tension effect, as well as for the contact angle effect. The viscosity ratio effect describes the effect of viscous fingering of the displacing fluid if the viscosity ratio

is low. The interfacial tension effect describes the trapping of displaced fluid within the pores if interfacial tension is increased. This is because the displacing fluid rather enters bigger pores due to the higher capillary pressure in the small pores and thereby leaves displaced fluid in the smaller pores behind (Gu, Liu, and Zhang 2018).

Chapter 6

References

- Carpenter, Chris. 2015. "Digital Rocks: Emerging Technology to Business-Proven Capability." *Journal of Petroleum Technology* 67 (08): 77-79. <https://doi.org/10.2118/0815-0077-JPT>.
- Collett, Timothy S. 2013. "Gas Hydrate Reservoir Properties." (URTEC-1579782-MS). <https://doi.org/10.1190/urtec2013-197>.
- Computer Modelling Group Ltd., CMG. 2016. STARS User Guide. In *Advanced Processes & Thermal Reservoir Simulator*.
- Delli, Mohana L., and Jocelyn L. H. Grozic. 2013. "Prediction Performance of Permeability Models in Gas-Hydrate-Bearing Sands." *SPE Journal* 18 (02): 274-284. <https://doi.org/10.2118/149508-PA>.
- Ecker, Christine, Jack Dvorkin, and Amos Nur. 1996. "Sediments With Gas Hydrates: Internal Structure From Seismic AVO." (SEG-1996-1767).
- Fu, Jinlong, Jiabin Dong, Yongliang Wang, Yang Ju, and D. Owen. 2020. "Resolution Effect: An Error Correction Model for Intrinsic Permeability of Porous Media Estimated from Lattice Boltzmann Method." *Transport in Porous Media* 132. <https://doi.org/10.1007/s11242-020-01406-z>.
- Geranutti, Bianca Levy Sgroi. 2020. "Investigation of gas hydrate formation during sea water injection based on undersaturated oil core flooding experiments."
- Gu, Qingqing, Haihu Liu, and Yonghao Zhang. 2018. "Lattice Boltzmann Simulation of Immiscible Two-Phase Displacement in Two-Dimensional Berea Sandstone." *Applied Sciences* 8 (9). <https://doi.org/10.3390/app8091497>.
- Hancock, Steven, Ray Boswell, and Tim Collett. 2019. "Development of Deepwater Natural Gas Hydrates." (D031S035R004). <https://doi.org/10.4043/29374-MS>.
- Herring, A. L., V. Robins, and A. P. Sheppard. 2019. "Topological Persistence for Relating Microstructure and Capillary Fluid Trapping in Sandstones." *Water Resources Research* 55 (1): 555-573. <https://doi.org/https://doi.org/10.1029/2018WR022780>.

- Kvenvolden, Keith A., and Thomas D. Lorenson. 2001. "Global Occurrences of Gas Hydrate." (ISOPE-I-01-069).
- Landry, Christopher J., Masa Prodanovic, Robert M. Reed, Peter Eichhubl, and Kishore Mohanty. 2017. "Estimating Oil-Water Relative Permeability Curves Using Digital Rock Physics." (URTEC-2691701-MS). <https://doi.org/10.15530/URTEC-2017-2691701>.
- Ma, Shouxiang, Guodong Jin, Rex Sy, and Hasan Kesserwan. 2018. "Rock Grain Size Prediction from NMR Measurement and Digital Rock Modeling- Experimental Validation." (SPE-192220-MS). <https://doi.org/10.2118/192220-MS>.
- Makogon, Y. F., S. A. Holditch, K. F. Perry, and J. C. Holste. 2004. "Gas Hydrate Deposits: Formation and Development." (OTC-16677-MS). <https://doi.org/10.4043/16677-MS>.
- Masalmeh, Shehadeh K., Xudong Jing, Sven Roth, Chenchen Wang, Hu Dong, and Martin Blunt. 2015. "Towards Predicting Multi-Phase Flow in Porous Media Using Digital Rock Physics: Workflow to Test the Predictive Capability of Pore-Scale Modeling." (D041S060R001). <https://doi.org/10.2118/177572-MS>.
- Meltser, A., D. Goldberg, and G. Guerin. 1999. Characterization of in situ elastic properties of gas hydrate-bearing sediments on the Blake Ridge. *JGR Solid Earth: J. Geophys. Res.*, 104(8), 17,781-17,795.
- Mohammadi, Amir Hossein, Hongyan Ji, Rod W. Burgass, Ali Bashir Ali, and Bahman Tohidi. 2006. "Gas Hydrates in Oil Systems." (SPE-99437-MS). <https://doi.org/10.2118/99437-MS>.
- Olofinnik, Oluwakemi. 2019. "Digital Rock Core Simulation of Waterflooding, Showing the Impact of Rock Heterogeneity on Oil Production." (D033S027R001). <https://doi.org/10.2118/198846-MS>.
- Rassenfoss, Stephen. 2011. "Digital Rocks Out to Become a Core Technology." *Journal of Petroleum Technology* 63 (05): 36-41. <https://doi.org/10.2118/0511-0036-JPT>.
- Reichel, Thomas, and Joseph W. Gallagher. 2014. "Global Screening of Gas Hydrates." (D041S048R002). <https://doi.org/10.4043/25144-MS>.
- Shabaninejad, Mehdi, Jill Middleton, and Andrew Fogden. 2018. "Systematic pore-scale study of low salinity recovery from Berea sandstone analyzed by micro-CT." *Journal of Petroleum Science and Engineering* 163: 283-294. <https://doi.org/https://doi.org/10.1016/j.petrol.2017.12.072>. <https://www.sciencedirect.com/science/article/pii/S092041051731029X>.
- Sloan, E. Dendy Jr. 1991. "Natural Gas Hydrates." *Journal of Petroleum Technology* 43 (12): 1414-1417. <https://doi.org/10.2118/23562-PA>.
- Tohidi Kalorazi, Bahman, and Ross Anderson. 2008. Methane from gas hydrates. In: Wall, J.D., et al., eds., *Bioenergy*. Washington, DC: ASM Press.
- Uddin, M., D. Coombe, D. Law, and B. Gunter. 2008. "Numerical Studies of Gas Hydrate Formation and Decomposition in a Geological Reservoir." *Journal of Energy Resources Technology* 130 (3). <https://doi.org/10.1115/1.2956978>.

-
- Yin, X., I. Zarihos, N. K. Karadimitriou, A. Raouf, and S. M. Hassanizadeh. 2019. "Direct simulations of two-phase flow experiments of different geometry complexities using Volume-of-Fluid (VOF) method." *Chemical Engineering Science* 195: 820-827. <https://doi.org/https://doi.org/10.1016/j.ces.2018.10.029>. <http://www.sciencedirect.com/science/article/pii/S0009250918307425>.
- Zhang, Hao, Peng Yuan, Jianghui Wu, Alberto Mezzatesta, Guodong Jin, Rajani Satti, Nils Koliha, Juan Bautista, Bernd Crouse, and David Freed. 2017. "Using Digital Rock Modeling to Estimate Permeability and Capillary Pressure from NMR and Geochemical Logs." (D041S041R002). <https://doi.org/10.2118/183883-MS>.